

# ALMA 0<sup>o</sup>.02-RESOLUTION OBSERVATIONS REVEAL HCN-ABUNDANCE-ENHANCED COUNTER-ROTATING AND OUTFLOWING DENSE MOLECULAR GAS AT THE NGC 1068 NUCLEUS

MASATOSHI IMANISHI,<sup>1,2</sup> DIEU D. NGUYEN,<sup>1</sup> KEIICHI WADA,<sup>3,4,5</sup> YOSHIAKI HAGIWARA,<sup>6,1</sup>  
SATORU IGUCHI,<sup>1,2</sup> TAKUMA IZUMI,<sup>1,2</sup> NOZOMU KAWAKATU,<sup>7</sup> KOUICHIRO NAKANISHI,<sup>1,2</sup> AND  
KYOKO ONISHI<sup>8</sup>

<sup>1</sup>*National Astronomical Observatory of Japan, National Institutes of Natural Sciences (NINS), 2-21-1 Osawa, Mitaka, Tokyo 181-8588, Japan*

<sup>2</sup>*Department of Astronomy, School of Science, The Graduate University for Advanced Studies, SOKENDAI, Mitaka, Tokyo 181-8588*

<sup>3</sup>*Kagoshima University, Graduate School of Science and Engineering, Kagoshima 890-0065, Japan*

<sup>4</sup>*Ehime University, Research Center for Space and Cosmic Evolution, Matsuyama 790-8577, Japan*

<sup>5</sup>*Hokkaido University, Faculty of Science, Sapporo 060-0810, Japan*

<sup>6</sup>*Natural Science Laboratory, Toyo University, 5-28-20 Hakusan, Bunkyo-ku, Tokyo 112-8606, Japan*

<sup>7</sup>*Faculty of Natural Sciences, National Institute of Technology, Kure College, 2-2-11 Agaminami, Kure, Hiroshima 737-8506, Japan*

<sup>8</sup>*Department of Space, Earth and Environment, Chalmers University of Technology, Onsala Space Observatory, SE-439 92 Onsala, Sweden*

(Received August 20, 2020)

Submitted to AAS

## ABSTRACT

We present ALMA  $\sim 0''.02$ -resolution observations of the nucleus of the nearby ( $\sim 14$  Mpc) type-2 AGN NGC 1068 at HCN/HCO<sup>+</sup>/HNC J=3–2 lines, as well as at their <sup>13</sup>C isotopologue and vibrationally excited lines, to scrutinize the morphological/dynamical/chemical/physical properties of dense molecular gas in the putative dusty molecular torus around a mass-accreting supermassive black hole. We confirm almost east-west-oriented dense molecular gas emission both morphologically and dynamically, which we regard as coming from the torus. Bright emission is compact ( $\lesssim 3$  pc), and low-surface-brightness emission extends out to 5–7 pc. These dense molecular gas properties are not symmetric between the eastern and western torus. The HCN J=3–2 emission is stronger than the HCO<sup>+</sup> J=3–2 emission within the  $\sim 7$  pc torus region, with an estimated dense molecular mass of  $(0.4\text{--}1.0)\times 10^6 M_{\odot}$ . We interpret that HCN abundance is enhanced in the torus. We detect signatures of outflowing dense molecular gas and a vibrationally excited HCN J=3–2 line. Finally, we find that in the innermost ( $\lesssim 1$  pc) part of the torus, the dense molecular line rotation velocity, relative to the systemic velocity, is the opposite of that in the outer ( $\gtrsim 2$  pc) part, in both the eastern and western torus. We prefer a scenario of counter-rotating dense molecular gas with innermost

almost-Keplerian-rotation and outer slowly rotating (far below Keplerian) components. Our high-spatial-resolution dense molecular line data reveal that torus properties of NGC 1068 are much more complicated than the simple axi-symmetrically rotating torus picture in the classical AGN unification paradigm.

## 1. INTRODUCTION

Active galactic nuclei (AGNs) are galaxy nuclei that shine very brightly from compact regions. The bright compact emission is believed to come from an actively mass-accreting supermassive black hole (SMBH) with mass of  $>10^6 M_{\odot}$ . Optical spectroscopy of AGNs has found that some display broad ( $\gtrsim 2000 \text{ km s}^{-1}$ ) emission lines (classified as type-1), while others show only narrow ( $\lesssim 1000 \text{ km s}^{-1}$ ) emission lines (type-2). It is now widely accepted that the presence of type-1 and -2 AGNs can naturally be explained by the presence of  $\lesssim$  a few 10 parsec (pc)-scale toroidally distributed dust and gas, the so-called dusty molecular torus, which surrounds a UV-optical-continuum-emitting accretion disk around an SMBH and the sub-pc-scale broad-line-emitting regions photo-ionized by the continuum emission (Antonucci 1993; Honig 2019). This AGN unification paradigm was originally proposed from observations of the nearby type-2 AGN, NGC 1068 ( $z \sim 0.0038$ , distance  $\sim 14 \text{ Mpc}$ , 1 arcsec is  $\sim 70 \text{ pc}$ ) (Antonucci & Miller 1985). Observationally scrutinizing the properties of the putative dusty molecular torus in NGC 1068 is an important first step toward understanding what the torus is and what its role is in AGNs. However, the apparent size of the putative  $\lesssim$  a few 10 pc-scale torus is small (e.g., 14 pc is 0<sup>′</sup>.2 at the distance of NGC 1068), so high-spatial-resolution observations are crucial to spatially resolving it clearly.

The use of ALMA has started to bring about significant advances in our understanding of the compact dusty molecular torus in NGC 1068. This is because high-spatial-resolution and high sensitivity data now can routinely be obtained at the (sub)millimeter wavelength, where rotational (J) transition lines of many abundant molecules are present. Garcia-Burillo et al. (2014) conducted  $\sim 0\text{′}.3\text{--}0\text{′}.5$ -resolution (sub)millimeter CO J=3–2/J=6–5 line and continuum observations of NGC 1068. Molecular line emission at the putative torus position overlapped brighter, surrounding spatially extended (50–150 pc scale) emission in the host galaxy, but these authors constrained torus properties by modeling continuum flux at multiple frequencies and CO data (e.g., torus mass is  $M_{\text{torus}} \sim \text{a few} \times 10^5 M_{\odot}$  and size is  $r_{\text{torus}} \sim 20 \text{ pc}$ ). This torus mass is much smaller than the SMBH mass of NGC 1068, with  $M_{\text{SMBH}} \sim 1 \times 10^7 M_{\odot}$ , which was estimated from  $\sim 22 \text{ GHz}$  ( $\sim 1.4 \text{ cm}$ ) H<sub>2</sub>O maser emission dynamics at  $\lesssim 1 \text{ pc}$ , constrained with Very Long Baseline Interferometry (VLBI) high-spatial-resolution ( $< 0\text{′}.01$ ) observations (Greenhill et al. 1996; Hure 2002; Lodato & Bertin 2003). Imanishi et al. (2016a) presented  $\sim 0\text{′}.1\text{--}0\text{′}.2$ -resolution HCN/HCO<sup>+</sup> J=3–2 line observations (i.e., dense molecular gas tracers), isolated compact dense molecular emission at the location of the putative torus from spatially extended (50–150 pc scale) brighter molecular emission, and estimated torus mass and size to be  $M_{\text{torus}} \sim \text{several} \times 10^5 M_{\odot}$  and  $r_{\text{torus}} \sim 10 \text{ pc}$ , respectively. The torus dynamics was still not clearly constrained owing to the lack of spatial resolution. Garcia-Burillo et al. (2016) and Gallimore et al. (2016) conducted  $\sim 0\text{′}.05\text{--}0\text{′}.08$ -resolution CO J=6–5 line observations of the NGC 1068 nucleus and revealed that molecular emission is morphologically elongated roughly along the east-west direction, but *observed* dynamical properties are dominated by almost north-south-oriented blueshifted and redshifted emission.

According to the classical torus picture, a torus is thought to rotate largely affected by the gravity of the central mass-dominating SMBH, because molecular viscosity is insufficient to remove angular momentum (e.g., Wada et al. 2009, 2016). In the case of NGC 1068, radio jet emission and optical [OIII] line emission photo-ionized by the AGN radiation extend to the north-south direction in the vicinity of the mass-accreting SMBH (Evans et al. 1991; Das et al. 2006; Gallimore et al. 2004). Since such emission can easily escape along a direction almost perpendicular to the putative dusty molecular

torus, the rotating torus in NGC 1068 is presumed to be located roughly along the east-west direction of the SMBH. In this case, both the molecular emission morphology and dynamics are expected to be aligned to the almost east-west direction. The observed north-south oriented velocity structure (Garcia-Burillo et al. 2016; Gallimore et al. 2016) is not easily reconciled with the classical torus picture. One possible scenario is that molecular outflow along the direction almost perpendicular to the torus is contributing greatly to the observed CO J=6–5 dynamics (Gallimore et al. 2016). It is also possible that the highly turbulent torus can create the observed north-south oriented velocity structure (Garcia-Burillo et al. 2016). The classical torus picture was not unambiguously demonstrated from observations.

Imanishi et al. (2018a) conducted ALMA  $\sim 0''.04\text{--}0''.07$  ( $2.8\text{ pc} \times 4.9\text{ pc}$ )-resolution observations of the NGC 1068 torus using dense molecular tracers, HCN/HCO<sup>+</sup> J=3–2 lines, and revealed almost east-west-oriented emission both morphologically and dynamically. This observational result conformed to what people had expected for the torus in NGC 1068. However, it was also found that (1) the velocity difference between the blueshifted and redshifted components at the probed physical scale ( $\sim 3\text{ pc}$ ) is much smaller than that expected from Keplerian rotation dominated by the central SMBH (see also Garcia-Burillo et al. (2016)), and (2) the dense molecular emission is *blueshifted* (*redshifted*) at the *western* (*eastern*) part of the torus, while both (a) innermost ( $\lesssim 1\text{ pc}$ )  $\sim 22\text{ GHz}$  H<sub>2</sub>O maser emission and (b) dense molecular emission in the host galaxy (50–150 pc scale) outside the torus, along the torus direction, showed *redshifted* (*blueshifted*) components at the *western* (*eastern*) part (Greenhill et al. 1996; Gallimore et al. 2004; Imanishi et al. 2018a). Dense molecular gas in the putative torus looked to be counter-rotating with respect to the innermost ( $\lesssim 1\text{ pc}$ ) H<sub>2</sub>O maser emission and outer (50–150 pc) host galaxy dense molecular gas. Figure 1 illustrates the observed complex dynamics of dense molecular gas at the NGC 1068 nucleus.

Impellizzeri et al. (2019) obtained ALMA  $\sim 0''.02$  ( $\sim 1.4\text{ pc}$ )-resolution HCN J=3–2 line data of the NGC 1068 torus and unveiled the presence of inner ( $\lesssim 2\text{ pc}$ ) and outer ( $\gtrsim 2\text{ pc}$ ) dynamically decoupled dense molecular gas components. The inner dense molecular gas displayed *redshifted* (*blueshifted*) motion at the *western* (*eastern*) part in a similar way to the innermost ( $\lesssim 1\text{ pc}$ ) H<sub>2</sub>O maser emission (Greenhill et al. 1996; Gallimore et al. 2004), while the outer one showed *blueshifted* (*redshifted*) motion at the *western* (*eastern*) side, as previously observed in  $\sim 0''.04\text{--}0''.07$ -resolution HCN/HCO<sup>+</sup> J=3–2 line data (Imanishi et al. 2018a). Impellizzeri et al. (2019) argued that two, almost-Keplerian, counter-rotating dense molecular gas components can explain these observational results. If this is the case, we are witnessing a very transient phase of the NGC 1068 torus, because such a counter-rotating molecular gas can quickly change to a co-rotating one. Garcia-Burillo et al. (2019) obtained  $\sim 0''.03\text{--}0''.09$ -resolution multiple molecular line data of the NGC 1068 torus, and preferred an outflow scenario rather than the counter-rotating molecular gas model, based mainly on detailed dynamical modeling and the expected very short time scale of the counter-rotating torus.

The observed properties of the NGC 1068 torus have been found to be far more complex and interesting than the classical torus picture of simple rotation governed by the central SMBH’s gravity. Further high-spatial-resolution molecular line data obtained with ALMA will help improve and refine our understanding of the torus in NGC 1068. In particular, one intriguing question is “Are the two dynamically decoupled torus molecular gas components found in HCN J=3–2 (Impellizzeri et al. 2019) also seen in other dense gas tracers?”. In this manuscript, we present the results of our ALMA

$\sim 0\prime.02$ -resolution observations of the NGC 1068 nucleus using dense gas tracers, HCN/HCO<sup>+</sup>/HNC J=3–2 lines, as well as their <sup>13</sup>C isotopologue and vibrationally excited lines.

Throughout this manuscript, “<sup>12</sup>C” is simply described as “C”, optical LSR velocity is adopted, and images of our newly taken ALMA data are displayed in ICRS coordinates, with north up and east to the left.

## 2. OBSERVATIONS AND DATA ANALYSES

Our ALMA band 6 (211–275 GHz) observations of the NGC 1068 nucleus were conducted through the Cycle 6 program 2018.1.00037.S (PI = M. Imanishi). The observation details are summarized in Table 1. Since our main interest is dense molecular gas properties of the compact torus, only long baselines were used.

We conducted two types of observations, one covering HCN/HCO<sup>+</sup> J=3–2 lines as well as their vibrationally excited (HCN-VIB/HCO<sup>+</sup>-VIB) J=3–2 lines (denoted as “data-a” in Table 1), and the other covering HNC, <sup>13</sup>C isotopologue (H<sup>13</sup>CN/H<sup>13</sup>CO<sup>+</sup>/HN<sup>13</sup>C) and HNC-VIB J=3–2 lines (denoted as “data-b”). In both observations, the phase center was the nucleus at (02<sup>h</sup> 42<sup>m</sup> 40.71<sup>s</sup>, –00° 00′ 47.94<sup>″</sup>)ICRS and we employed the widest 1.875 GHz-width mode in each spectral window. For data-a, we took spectra at 263.6–269.1 GHz, with three spectral windows to cover HCN J=3–2 ( $\nu_{\text{rest}} = 265.886$  GHz) and HCO<sup>+</sup> J=3–2 ( $\nu_{\text{rest}} = 267.558$  GHz) lines, as well as vibrationally excited HCN  $v_2=1, l=1f$  (HCN-VIB) J=3–2 ( $\nu_{\text{rest}} = 267.199$  GHz) and HCO<sup>+</sup>  $v_2=1, l=1f$  (HCO<sup>+</sup>-VIB) J=3–2 ( $\nu_{\text{rest}} = 268.689$  GHz) lines. For data-b, we took spectra at 256.7–260.5 GHz, with two spectral windows in LSB to cover H<sup>13</sup>CN J=3–2 ( $\nu_{\text{rest}} = 259.012$  GHz), H<sup>13</sup>CO<sup>+</sup> J=3–2 ( $\nu_{\text{rest}} = 260.255$  GHz), and HN<sup>13</sup>C J=3–2 ( $\nu_{\text{rest}} = 261.263$  GHz) lines. In USB, we covered 270.0–273.7 GHz with two spectral windows to include HNC J=3–2 ( $\nu_{\text{rest}} = 271.981$  GHz) and HNC  $v_2=1, l=1f$  (HNC-VIB) J=3–2 ( $\nu_{\text{rest}} = 273.870$  GHz) lines. Since HNC and <sup>13</sup>C isotopologue J=3–2 lines are fainter than HCN/HCO<sup>+</sup> J=3–2 lines, we set the beam size requested in our program slightly larger for data-b ( $\sim 0\prime.03$ ) than that for data-a ( $\sim 0\prime.02$ ).

For our data reduction, we used CASA (<https://casa.nrao.edu>) starting from calibrated data provided by ALMA. We first determined a constant continuum flux level by using data that were not affected by emission and absorption lines, and used the CASA task “uvcontsub” to subtract the derived continuum emission from the data. We then applied the task “clean” (Briggs-weighting; robust=0.5, gain = 0.1) to the continuum-subtracted molecular line data as well as the extracted continuum data. The adopted velocity resolution was 10–20 km s<sup>–1</sup>. The pixel scale was 0<sup>′</sup>003 pixel<sup>–1</sup> and 0<sup>′</sup>005 pixel<sup>–1</sup> for data-a and -b, respectively. The maximum recoverable scale (MRS) is 0<sup>′</sup>24–0<sup>′</sup>30 and 0<sup>′</sup>56–0<sup>′</sup>62 for data-a and -b, respectively. Emission with a spatial extent larger than these MRSs may be resolved out and may not be recovered in our ALMA data. The absolute flux calibration uncertainty is expected to be <10% at the observed frequencies in our ALMA Cycle 6 data.

## 3. RESULTS

Continuum emission at  $\sim 260$  GHz ( $\sim 1.2$  mm) at the NGC 1068 nucleus taken in data-a is displayed as contours in Figure 2. Table 2 summarizes the continuum emission properties at the NGC 1068 nucleus. Although the continuum emission looks spatially compact, its flux is slightly ( $\sim 26\%$ ) larger in  $\sim 0\prime.03$ -resolution data-b (8.2 mJy beam<sup>–1</sup>) than in  $\sim 0\prime.02$ -resolution data-a (6.5 mJy beam<sup>–1</sup>), suggesting that continuum emission is spatially extended ( $\gtrsim 0\prime.02$  or  $\gtrsim 1.4$  pc). Spa-

tially extended, radio-jet-related synchrotron emission (Garcia-Burillo et al. 2019), free-free emission (Impellizzeri et al. 2019), and/or dust emission in the torus at  $\gtrsim 1.4$  pc may contribute to the observed continuum flux of  $\sim 0''.03$ -resolution data-b. We modified the beam size of data-a to match that of data-b, using the CASA task “imsmooth”, and confirmed that the continuum peak flux of data-a became  $8.1$  ( $\text{mJy beam}^{-1}$ ) ( $54\sigma$ ), which agrees well with that of data-b ( $8.2$   $\text{mJy beam}^{-1}$ ).

The integrated intensity (moment 0) maps of the HCN J=3–2 and HCO<sup>+</sup> J=3–2 lines are shown in Figure 2 (top panels). We adopt the  $\sim 260$  GHz continuum peak position as the location of the mass-accreting SMBH, because this position spatially agrees with continuum peaks derived in other high-spatial-resolution ( $< 0''.1$ ) (sub)millimeter–centimeter observations at 5–700 GHz (Gallimore et al. 2004; Garcia-Burillo et al. 2019). Both the HCN J=3–2 and HCO<sup>+</sup> J=3–2 line emission are clearly detected along the almost east-west direction, relative to the active SMBH position, with the western side being significantly brighter than the eastern side, as previously seen in  $\sim 0''.04 \times 0''.07$ -resolution ALMA data (Imanishi et al. 2018a). We interpret this to mean that the emission originates in the putative torus in NGC 1068. Table 3 summarizes more detailed properties of dense molecular line emission in the torus region.

The dense molecular line emission is particularly bright in a relatively compact area within  $\sim 3$  pc in both the west and east (Figure 2a,b). In addition to this compact component, low-surface-brightness emission extends out to 5–7 pc, particularly in HCN J=3–2. Significantly detected emission of HCN J=3–2 is spatially more extended than that of HCO<sup>+</sup> J=3–2, despite larger noise in the former (Table 3, column 4). The size of  $\lesssim 7$  pc is much smaller than the size of the CO J=3–2 and J=2–1 emitting region ( $\sim 25$ – $30$  pc), which probes less dense and cooler molecular gas (Garcia-Burillo et al. 2019). Dense and warm molecular gas that can excite HCN and HCO<sup>+</sup> to the J=3 level is mostly concentrated in  $\lesssim 7$  pc area in the NGC 1068 torus.

The intensity-weighted mean velocity (moment 1) maps of the HCN J=3–2 and HCO<sup>+</sup> J=3–2 lines are also displayed in Figure 2 (bottom panels). The velocity display range is set as the same as that adopted in the  $\gtrsim 0''.04$ -resolution moment 1 maps of the same molecular lines by Imanishi et al. (2018a), in order to compare velocity patterns between our new  $\sim 0''.02$ -resolution and old  $\gtrsim 0''.04$ -resolution data. To discuss the dynamics of dense molecular emission in the torus, we adopt the systemic velocity of NGC 1068 to be  $V_{\text{sys}} = 1130$   $\text{km s}^{-1}$  in the optical LSR velocity ( $z \sim 0.0038$ ), because nuclear HCN J=3–2 and HCO<sup>+</sup> J=3–2 emission lines showed velocity peaks around this value (Imanishi et al. 2016a, 2018a; Impellizzeri et al. 2019). Imanishi et al. (2018a) found that both the HCN J=3–2 and HCO<sup>+</sup> J=3–2 line emission are blueshifted in the western torus at  $\lesssim 5$  pc and redshifted in the eastern torus at  $\lesssim 5$  pc. The implied rotation velocity was substantially slower than that expected for Keplerian rotation ( $\pm 120$   $\text{km s}^{-1}$  at  $\sim 3$  pc) for the central mass-dominating compact SMBH with mass of  $M_{\text{SMBH}} \sim 1 \times 10^7 M_{\odot}$  (Greenhill et al. 1996; Hure 2002; Lodato & Bertin 2003), unless we view the torus dense molecular gas rotation from a nearly face-on direction. This would be very unlikely for the type-2 AGN NGC 1068, because it is expected to be obscured by the fairly edge-on, east-west-oriented torus. In our new  $\sim 0''.02$ -resolution moment 1 map of the HCN J=3–2 line (Figures 2c), western blueshifted and eastern redshifted motions are clearly confirmed at  $\gtrsim 2$  pc from the SMBH along the position angle PA  $\sim 105$ – $110^{\circ}$  east of north (Imanishi et al. 2018a). The velocity difference with respect to the systemic is only  $\lesssim 50$   $\text{km s}^{-1}$ , which is still much smaller than that expected from Keplerian rotation.



It is also found that *innermost* ( $\lesssim 1$  pc) dense molecular emission is redshifted on the western side and blueshifted on the eastern side, the opposite of what is found in the outer torus ( $\gtrsim 2$  pc) emission. This pattern is clearly seen, particularly in the HCN J=3–2 line data (Figure 2c), and was previously detected by Impellizzeri et al. (2019) in the same line data. Our new data reveal that western redshifted and eastern blueshifted *innermost* components are also seen in the HCO<sup>+</sup> J=3–2 line (Figure 2d), suggesting that this innermost torus dynamics is characteristic of dense molecular gas in NGC 1068.

Figure 3 (top panels) shows the intensity-weighted mean velocity (moment 1) maps of HCN J=3–2 and HCO<sup>+</sup> J=3–2, with a wider velocity range. We see redshifted high-velocity components at the innermost western torus, in both the HCN J=3–2 and HCO<sup>+</sup> J=3–2 emission lines. Intensity-weighted velocity dispersion (moment 2) maps are displayed in Figure 3 (bottom panels). High velocity dispersion regions are seen in the western torus in both the lines, as previously found in  $\gtrsim 0\prime.04$ -resolution maps (Imanishi et al. 2018a). In the new  $\sim 0\prime.02$ -resolution data, it becomes clear for the first time that the highest-velocity dispersion spot in the moment 2 map is shifted toward the outer northwestern side of the innermost redshifted high-velocity component in the moment 1 map.

Figure 4 (top panels) shows spectra, within the beam size, at the position of the continuum peak (hereafter, “C-peak”; [02<sup>h</sup> 42<sup>m</sup> 40.709<sup>s</sup>, –00° 00′ 47.946<sup>″</sup>]), the HCN J=3–2 emission peak in the eastern torus (hereafter, “E-peak”; [02<sup>h</sup> 42<sup>m</sup> 40.710<sup>s</sup>, –00° 00′ 47.952<sup>″</sup>]), and the HCN J=3–2 emission peak in the western torus (hereafter, “W-peak”; [02<sup>h</sup> 42<sup>m</sup> 40.708<sup>s</sup>, –00° 00′ 47.940<sup>″</sup>]), derived from Figure 2a. Both HCN J=3–2 and HCO<sup>+</sup> J=3–2 lines are clearly detected in emission at the E- and W-peaks, but in absorption at the C-peak. Gaussian fits to several clearly detected emission lines are shown in Figure 5, and estimated molecular line fluxes are tabulated in Table 3. The molecular line widths are larger in the W-peak than in the E-peak, suggesting larger turbulence at the W-peak. Figure 6 displays the velocity profiles of the HCN J=3–2 and HCO<sup>+</sup> J=3–2 lines at the C-peak.

To investigate overall molecular emission line properties in a larger volume of the torus, we also extract area-integrated spectra within (a) a 0<sup>′</sup>.2 (east-west)  $\times$  0<sup>′</sup>.1 (north-south) (14 pc  $\times$  7 pc) rectangular region (i.e., covering both the eastern and western torus), (b) a 0<sup>′</sup>.1  $\times$  0<sup>′</sup>.1 (7 pc  $\times$  7 pc) square region of the eastern torus (hereafter, “E-torus”), and (c) the same square region of the western torus (hereafter, “W-torus”). Figure 7 displays these area-integrated spectra. Gaussian fits are applied to estimate the fluxes of these emission lines (Figure 8 and Table 4). The molecular line widths are larger in the W-torus than in the E-torus (Table 4), confirming that higher turbulence happens in the W-torus, as suggested from the higher velocity dispersion values there in moment 2 maps (Figure 3c,d).

For the HCN J=3–2 line, Impellizzeri et al. (2019) obtained ALMA Cycle 5 data with spatial resolution ( $\sim 0\prime.02$ ) comparable to ours. We combined our Cycle 6 and their Cycle 5 data and show several selected results in Appendix A. Main features detected in our Cycle 6 data are reproduced in the combined data as well. To compare the observed properties of HCN J=3–2 and other lines in a uniform manner, we use the results obtained with our Cycle 6 data only, because we want to avoid possible systematic uncertainties resulting from combining data taken with largely different observing parameters.

Beam-sized spectra of data-b (<sup>13</sup>C isotopologue and HNC J=3–2 observations) at the same three positions (C-, E-, and W-peaks) are displayed in Figure 4d–4i. Figure 9 displays the moment 0 maps of the H<sup>13</sup>CN J=3–2, HNC J=3–2, and H<sup>13</sup>CO<sup>+</sup> J=3–2 lines. A  $>3\sigma$  signal is detected either in

emission or absorption in the torus region for  $\text{H}^{13}\text{CN}$  J=3–2 and  $\text{HNC}$  J=3–2 (Table 3), while no significant signal is recognizable for  $\text{H}^{13}\text{CO}^+$  J=3–2 ( $<3\sigma$ ). The  $\text{H}^{13}\text{CN}$  J=3–2 line velocity profiles at the C- and W-peaks are shown in Figure 10.

For the  $\text{HCN}$  J=3–2 and  $\text{HCO}^+$  J=3–2 emission lines from the torus, we compare their fluxes in our Cycle 6 data and previously taken Cycles 4 and 2 data that include shorter baselines (Imanishi et al. 2018a). We found that their fluxes roughly agree (Appendix B), supporting our view that we recover virtually all dense molecular line emission flux from the torus in our Cycle 6 data. However, for spatially extended emission components in the host galaxy, the recovered fluxes of  $\text{HCN}$  J=3–2 and  $\text{HCO}^+$  J=3–2 lines in the Cycle 6 data were found to be substantially smaller than those in the Cycles 4 and 2 data (Imanishi et al. 2018a). We will thus discuss only compact torus emission.

## 4. DISCUSSION

### 4.1. *HCN-abundance-enhanced dense molecular torus*

It was found from lower-spatial-resolution ( $\gtrsim 0''.04$ ) molecular line observations that  $\text{HCN}$  emission is stronger than the  $\text{HCO}^+$  emission in the NGC 1068 torus region within  $<10$  pc from the central AGN (Garcia-Burillo et al. 2014; Viti et al. 2014; Imanishi et al. 2016a, 2018a). Thanks to our high-spatial-resolution ( $\sim 0''.02$  or  $\sim 1.4$  pc) data, we can now investigate dense molecular emission line properties in detail in the eastern and western torus separately. We find that the emission line flux of  $\text{HCN}$  J=3–2 is a factor of  $\sim 1.5$  higher than that of  $\text{HCO}^+$  J=3–2 in both the W- and E-torus (Table 4).

Elevated  $\text{HCN}$  emission, relative to  $\text{HCO}^+$  emission, is often found in luminous AGNs, compared with starburst-dominated regions (e.g., Kohno 2005; Imanishi et al. 2006b, 2007b; Krips et al. 2008; Imanishi et al. 2009; Privon et al. 2015; Izumi et al. 2016; Imanishi et al. 2016c, 2018b, 2019). An enhanced  $\text{HCN}$  abundance by AGN radiation (e.g., Kohno 2005; Imanishi et al. 2007b; Yamada et al. 2007; Izumi et al. 2016) and/or mechanical (Izumi et al. 2013; Martin et al. 2015) effects is proposed to be the physical origin. We thus investigate an  $\text{HCN}$ -to- $\text{HCO}^+$  abundance ratio in the NGC 1068 torus based on our ALMA Cycle 6 data.

Since the emission lines of the abundant  $\text{HCN}$  and  $\text{HCO}^+$  can be optically thick in the nuclear regions of active galaxies (e.g., Jiang et al. 2011; Jimenez-Donaire et al. 2017), it is not straightforward to convert from the observed  $\text{HCN}$ -to- $\text{HCO}^+$  J=3–2 flux ratio to an  $\text{HCN}$ -to- $\text{HCO}^+$  abundance ratio. We thus use the isotopologue  $\text{H}^{13}\text{CN}$  J=3–2 and  $\text{H}^{13}\text{CO}^+$  J=3–2 line data to constrain the  $\text{HCN}$ -to- $\text{HCO}^+$  abundance ratio, because the  $^{13}\text{C}$  isotopologue molecular abundance is usually  $\gtrsim 10$  times smaller (Aladro et al. 2015) and so the isotopologue lines are more likely to be optically thin. Unfortunately, these isotopologue  $\text{H}^{13}\text{CN}$  and  $\text{H}^{13}\text{CO}^+$  emission lines are much fainter than the  $\text{HCN}$  and  $\text{HCO}^+$  lines. We detect no clear isotopologue emission line in the W- and E-peaks ( $<3\sigma$ ), but identify a significant ( $\sim 4.5\sigma$ ) negative absorption signal with  $-0.090$  ( $\text{Jy beam}^{-1} \text{ km s}^{-1}$ ) at the C-peak in the  $\text{H}^{13}\text{CN}$  J=3–2 moment 0 map (Figure 9a). No significant absorption is recognizable at the C-peak in the  $\text{H}^{13}\text{CO}^+$  J=3–2 moment 0 map ( $<2\sigma$  or  $> -0.049$  [ $\text{Jy beam}^{-1} \text{ km s}^{-1}$ ] in Figure 9c), suggesting that the  $\text{H}^{13}\text{CN}$  column density is higher than  $\text{H}^{13}\text{CO}^+$  in the molecular gas in front of the  $\sim 260$ -GHz-continuum-emitting region. Assuming that this absorbing molecular gas largely comes from the nearly edge-on dusty molecular torus at the foreground side of the central mass-accreting SMBH, the observed  $\text{H}^{13}\text{CN}$ -to- $\text{H}^{13}\text{CO}^+$  J=3–2 absorption signal ratio with  $>1.8$  suggests an enhanced  $\text{HCN}$  abundance, relative to  $\text{HCO}^+$ , in the NGC 1068 torus, where we assume that the



$\text{H}^{13}\text{CN}$ -to- $\text{H}^{13}\text{CO}^+$  column density ratio (= abundance ratio) is comparable to an  $\text{HCN}$ -to- $\text{HCO}^+$  abundance ratio.

More precisely, an Einstein B-coefficient and excitation effect need to be taken into account to discuss a column density ratio (= an abundance ratio) based on an absorption strength.  $\text{H}^{13}\text{CN}$   $J=3-2$  and  $\text{H}^{13}\text{CO}^+$   $J=3-2$  absorption features can be detected when millimeter  $\sim 259$  GHz and  $\sim 260$  GHz photons are absorbed by  $\text{H}^{13}\text{CN}$  and  $\text{H}^{13}\text{CO}^+$  at the  $J=2$  level, respectively, and are used for excitation to the  $J=3$  level. The B-coefficient from  $J=2$  to  $J=3$  ( $B_{23}$ ) of  $\text{H}^{13}\text{CO}^+$  is a factor of  $\sim 1.7$  higher than that of  $\text{H}^{13}\text{CN}$ , based on data from the Cologne Database of Molecular Spectroscopy (CDMS) (Müller et al. 2005) via Splatalogue (<http://www.splatalogue.net>). Thus, for the same column density, an absorption strength can be a factor of  $\sim 1.7$  stronger for  $\text{H}^{13}\text{CO}^+$   $J=3-2$  than for  $\text{H}^{13}\text{CN}$   $J=3-2$ , as long as these lines are optically thin. Additionally, the critical density of  $\text{H}^{13}\text{CO}^+$  is a factor of  $\sim 5$  smaller than that of  $\text{H}^{13}\text{CN}$  for the same  $J$ -transition under the same temperature and line opacity (Shirley 2015). We ran RADEX calculations (van der Tak et al. 2007) and found that for a volume number density of  $10^{4-6}$  ( $\text{cm}^{-3}$ ), column density of  $10^{14-15}$  ( $\text{cm}^{-2}$ )<sup>1</sup>, kinetic temperature of 30–100 (K), and line width of 200–300 ( $\text{km s}^{-1}$ ),  $\text{H}^{13}\text{CO}^+$  is excited to  $J=2$  more than  $\text{H}^{13}\text{CN}$  is. Considering these two factors (i.e., B-coefficient and excitation), we derive a column density of  $\text{H}^{13}\text{CN}$  that is a factor of  $>3$  ( $>1.8 \times 1.7$ ) higher than that of  $\text{H}^{13}\text{CO}^+$ , or an  $\text{HCN}$ -to- $\text{HCO}^+$  abundance ratio of  $>3$ , in the NGC 1068 torus. Theoretically, an  $\text{HCN}$  abundance enhancement around a luminous AGN is predicted in some, but not all, parameter ranges, and so is not uncontroversially predicted (Meijerink & Spaans 2005; Meijerink et al. 2007; Harada et al. 2013; Viti 2017). However, observations of molecular gas in the vicinity of luminous AGNs suggest an enhanced  $\text{HCN}$  abundance in almost all cases (e.g., Sternberg et al. 1994; Aladro et al. 2015; Nakajima et al. 2018; Imanishi et al. 2018b; Saito et al. 2018; Kamenno et al. 2020; Takano et al. 2020). We argue that this is also the case for the NGC 1068 torus.

In the widely accepted molecular gas model in galaxies (Solomon et al. 1987), a molecular cloud consists of compact dense clumps with a small volume-filling factor. Each clump can be optically thick for  $\text{HCN}$   $J=3-2$  and  $\text{HCO}^+$   $J=3-2$  lines and is randomly moving. Molecular emission lines from clumps at the far side of the molecular cloud can escape toward Earth if their velocity is different from the foreground clumps inside the cloud. If an abundance is higher for  $\text{HCN}$  than  $\text{HCO}^+$ , flux attenuation by line opacity of foreground clumps is likely to be higher for  $\text{HCN}$   $J=3-2$  than  $\text{HCO}^+$   $J=3-2$ . In a more highly turbulent region, the  $\text{HCN}$   $J=3-2$  flux can increase more than the  $\text{HCO}^+$   $J=3-2$  flux, because of larger reduction of line opacity by foreground clumps in the former. In fact,  $\text{HCN}$ -to- $\text{HCO}^+$   $J=3-2$  flux ratio at the highly turbulent W-peak ( $\sim 1.5$ ; Table 3) is higher than that ( $\sim 1$ ) at the less turbulent E-peak. Figure 11 displays an  $\text{HCN}$ -to- $\text{HCO}^+$   $J=3-2$  flux ratio in the overall bright compact ( $\lesssim 3$  pc) torus region. The flux ratio tends to be systematically higher in the more turbulent W-torus than the E-torus, as expected from the enhanced  $\text{HCN}$  abundance scenario.

The observed wider spatial extent of  $\text{HCN}$   $J=3-2$  than  $\text{HCO}^+$   $J=3-2$  in the NGC 1068 torus region (Figures 2a,b) can also be a natural consequence of the enhanced  $\text{HCN}$  abundance. Because the critical density of  $\text{HCO}^+$   $J=3-2$  is a factor of  $\sim 5$  smaller than that of  $\text{HCN}$   $J=3-2$  (Shirley 2015),

<sup>1</sup> We assume the hydrogen column density in the NGC 1068 torus to be  $N_{\text{H}} \sim 10^{24-25}$   $\text{cm}^{-2}$ , because the estimated high value of  $N_{\text{H}} \sim 10^{25}$   $\text{cm}^{-2}$  (Matt et al. 1997; Bauer et al. 2015; Marinucci et al. 2016) is toward a compact X-ray emitting source, and  $N_{\text{H}}$  in other directions can be smaller in the case of a clumpy molecular gas structure (see §4.5). Adopting a factor of 4–5 enhanced  $\text{HCN}$ -to- $\text{H}_2$  abundance ratio of  $10^{-8}$ , compared to the canonical ratio of a few  $\times 10^{-9}$  observed in active galaxies (e.g., Martin et al. 2006; Saito et al. 2018) and a  $^{12}\text{C}$ -to- $^{13}\text{C}$  abundance ratio of  $\sim 30$ – $100$  (e.g., Henkel & Mauersberger 1993; Henkel et al. 1993; Martin et al. 2010; Henkel et al. 2014), we obtain the  $\text{H}^{13}\text{CN}$  and  $\text{H}^{13}\text{CO}^+$  column density in the NGC 1068 torus to be  $\sim 10^{14-15}$  ( $\text{cm}^{-2}$ )

under the same abundance, the HCO<sup>+</sup> J=3–2 line emission shows higher flux than HCN J=3–2 everywhere, and the emission size of HCO<sup>+</sup> is usually larger than HCN at the same J-transition line (Imanishi et al. 2007b; Saito et al. 2015, 2018; Imanishi et al. 2019). Emission from a highly abundant molecule (i.e., HCN) is still detectable from less dense and cooler molecular gas outside the compact ( $\lesssim 3$  pc) main torus of NGC 1068 (Garcia-Burillo et al. 2019).

Summarizing, various observational results described in this section consistently suggest an enhanced HCN abundance, relative to HCO<sup>+</sup>, in the NGC 1068 torus.

#### 4.2. Estimated torus dense molecular mass

We can estimate HCN J=3–2 and HCO<sup>+</sup> J=3–2 emission line luminosity from their fluxes within the 14 pc  $\times$  7 pc torus region (Table 4), using the following equations (Solomon & Vanden Bout 2005),

$$\left(\frac{L_{line}}{L_{\odot}}\right) = 1.04 \times 10^{-3} \left(\frac{\nu_{rest}}{\text{GHz}}\right) (1+z)^{-1} \left(\frac{D_L}{\text{Mpc}}\right)^2 \left(\frac{S\Delta V}{\text{Jy km s}^{-1}}\right) \quad (1)$$

and

$$\left(\frac{L'_{line}}{\text{K km s}^{-1} \text{ pc}^2}\right) = 3.25 \times 10^7 \left(\frac{\nu_{rest}}{\text{GHz}}\right)^{-2} (1+z)^{-1} \left(\frac{D_L}{\text{Mpc}}\right)^2 \left(\frac{S\Delta V}{\text{Jy km s}^{-1}}\right), \quad (2)$$

where  $S\Delta V$  is the Gaussian-fit, velocity-integrated line flux and  $D_L$  is the luminosity distance. Table 5 summarizes the derived luminosity. Assuming that HCN and HCO<sup>+</sup> emission in the dense and warm NGC 1068 torus is almost thermalized at up to J=3 and optically thick at J=3–2 and lower J-transitions, then the J=1–0 luminosity within the same area (in K km s<sup>−1</sup> pc<sup>2</sup>) is expected to be comparable to the J=3–2 luminosity; namely, HCN J=1–0 and HCO<sup>+</sup> J=1–0 emission line luminosity is  $L'_{\text{HCN J=1–0}} \sim 3.1 \times 10^5$  (K km s<sup>−1</sup> pc<sup>2</sup>) and  $L'_{\text{HCO}^+ \text{ J=1–0}} \sim 2.0 \times 10^5$  (K km s<sup>−1</sup> pc<sup>2</sup>), respectively. Using the conversion from (optically thick) HCN J=1–0 luminosity to dense molecular hydrogen (H<sub>2</sub>) mass,  $M_{\text{dense-H}_2}(\text{HCN}) = 6\text{--}12 \times \text{HCN J=1–0 luminosity (M}_{\odot} [\text{K km s}^{-1} \text{ pc}^2]^{-1})$  (Gao & Solomon 2004; Krips et al. 2008; Leroy et al. 2017), we obtain HCN-derived dense H<sub>2</sub> mass within the 14 pc  $\times$  7 pc torus region to be  $M_{\text{dense-H}_2}(\text{HCN}) = 2\text{--}4 \times 10^6 M_{\odot}$ . The dense H<sub>2</sub> mass can also be derived from HCO<sup>+</sup> data to be  $M_{\text{dense-H}_2}(\text{HCO}^+) = 0.4\text{--}1.0 \times 10^6 M_{\odot}$ , where the relation of  $M_{\text{dense-H}_2}(\text{HCO}^+) = 2\text{--}5 \times \text{HCO}^+ \text{ J=1–0 luminosity (M}_{\odot} [\text{K km s}^{-1} \text{ pc}^2]^{-1})$  in an optically thick regime (Leroy et al. 2017) is adopted. The derived masses are also summarized in Table 5. These H<sub>2</sub> masses include the compact ( $\lesssim 3$  pc) main torus component with bright, high-surface-brightness dense molecular line emission (Figure 2a,b) and a spatially extended (3–7 pc) low-surface-brightness emission component just outside the main torus.

The dense H<sub>2</sub> mass derived from HCN is a factor of  $\sim 4\text{--}5$  higher than the one derived from HCO<sup>+</sup>, where a standard HCN-to-H<sub>2</sub> and HCO<sup>+</sup>-to-H<sub>2</sub> abundance ratio observed in galaxies is implicitly assumed. The HCN J=3–2 line flux is also a factor of  $\sim 1.5$  higher than the HCO<sup>+</sup> J=3–2 line flux in all the area-integrated torus spectra in Figure 8 (Table 4). To explain an HCN-to-HCO<sup>+</sup> J-transition line flux ratio significantly higher than unity in the vicinity of a luminous AGN, an HCN-to-HCO<sup>+</sup> *abundance* ratio much higher than its *flux* ratio is required theoretically, because rotational (J) excitation is generally more difficult in HCN, due to higher critical density, than in HCO<sup>+</sup> (Yamada et al. 2007; Izumi et al. 2016). The fact that (1) the HCN-derived dense H<sub>2</sub>

mass is a factor of  $\sim 4$ – $5$  higher than the  $\text{HCO}^+$ -derived mass and (2) the  $\text{HCN}$   $J=3-2$  emission line flux is a factor of  $\sim 1.5$  higher than that of  $\text{HCO}^+$   $J=3-2$  can naturally be explained by the enhanced  $\text{HCN}$  abundance scenario <sup>2</sup> in the NGC 1068 torus (§4.1). By considering the suggested  $\text{HCN}$  overabundance and the resulting possible overestimation of  $\text{HCN}$ -derived  $\text{H}_2$  mass, we adopt the  $\text{HCO}^+$ -derived torus dense  $\text{H}_2$  mass of  $M_{\text{dense-H}_2}(\text{torus}) \sim 0.4\text{--}1.0 \times 10^6 M_\odot$  for our subsequent discussion.

In this  $\text{HCO}^+$ -based torus dense molecular mass estimate, it is assumed that  $\text{HCO}^+$  is excited by  $\text{H}_2$  molecules in a wide volume number density range (Leroy et al. 2017), while it is often assumed that  $\text{HCO}^+$  is primarily excited by  $\text{H}_2$  molecules whose volume number density is as high as the critical density. If we simply regard that the  $\text{HCO}^+$   $J=3-2$  emission preferentially probes dense molecular gas with  $\sim 10^6 \text{ cm}^{-3}$ , close to the  $\text{HCO}^+$   $J=3-2$  critical density (Shirley 2015), the emitting size of the  $0.4\text{--}1.0 \times 10^6 M_\odot$  gas is estimated to be  $\sim 3\text{--}6$  pc, where a spherical distribution with a dense molecular clump volume-filling factor of  $\sim 0.01\text{--}0.1$  (Wada & Norman et al. 2007; Wada 2012) is assumed (see also §4.5). This estimated size is roughly comparable to the observed size of the high-surface-brightness  $\text{HCO}^+$   $J=3-2$  emission in the main torus component (Figure 2b). This independent, simple comparison also suggests that the estimated torus dense molecular mass is reasonable. Our adopted torus mass of  $M_{\text{dense-H}_2}(\text{torus}) \sim 0.4\text{--}1.0 \times 10^6 M_\odot$  also roughly agrees with the recent updated estimate by Garcia-Burillo et al. (2019) based on high-spatial-resolution (0′03–0′09) ALMA data ( $\sim 0.3 \times 10^6 M_\odot$ ), and is significantly smaller than the central SMBH mass with  $M_{\text{SMBH}} \sim 1 \times 10^7 M_\odot$  (Greenhill et al. 1996; Hure 2002; Lodato & Bertin 2003).

#### 4.3. Redshifted dense molecular emission from the innermost northwestern torus

The moment 1 maps of  $\text{HCN}$   $J=3-2$  and  $\text{HCO}^+$   $J=3-2$  in Figure 3a,b show a redshifted, high-velocity emission component at the innermost ( $\lesssim 1$  pc) part of the northwestern torus, with this signature being much clearer for  $\text{HCN}$   $J=3-2$  than  $\text{HCO}^+$   $J=3-2$ . Redshifted  $\sim 22$  GHz ( $\sim 1.4$  cm)  $\text{H}_2\text{O}$  maser emission was also detected with VLBI very-high-spatial-resolution observations, at  $0.6\text{--}1.1$  pc on the northwestern side of the mass-accreting SMBH (Greenhill et al. 1996; Greenhill & Gwinn 1997). It is interesting to compare our ALMA-detected, redshifted dense molecular line emission with the VLBI-detected  $\text{H}_2\text{O}$  maser emission.

The  $\sim 22$  GHz ( $\sim 1.4$  cm)  $\text{H}_2\text{O}$  maser emission shows a declining rotation curve, indicative of an almost edge-on rotating disk, and is fitted with a slightly sub-Keplerian motion of  $V \propto r^{-0.31}$ , with the estimated central SMBH mass of  $M_{\text{SMBH}} \sim 1 \times 10^7 M_\odot$  (Greenhill et al. 1996; Greenhill & Gwinn 1997), where  $V$  is velocity and  $r$  is the distance from the central mass-dominating SMBH. Figure 12 displays velocity properties of the  $\text{HCN}$   $J=3-2$  and  $\text{HCO}^+$   $J=3-2$  emission lines along the northwest direction from the SMBH, overplotted with (1) Keplerian rotation ( $V \propto r^{-0.5}$ ) dominated by a point source with mass of  $1 \times 10^7 M_\odot$ , and (2) the slightly sub-Keplerian motion ( $V \propto r^{-0.31}$ ) derived from the  $\text{H}_2\text{O}$  maser emission (Greenhill & Gwinn 1997). Our ALMA data demonstrate that  $\text{HCN}$   $J=3-2$  and  $\text{HCO}^+$   $J=3-2$  emission line dynamics roughly agrees with the VLBI-detected  $\text{H}_2\text{O}$  maser dynamics at  $< 0.7$  pc. It is thus reasonable to interpret that  $\text{H}_2\text{O}$ ,  $\text{HCN}$   $J=3-2$ , and  $\text{HCO}^+$   $J=3-2$

<sup>2</sup> If a molecular cloud consists of randomly moving, compact dense clumps with a small volume-filling factor (Solomon et al. 1987), increased abundance of a certain molecule will result in the increase of its emission line flux from a molecular cloud, even if individual clumps are optically thick. This is because the  $\tau=1$  sphere in each clump moves outward and an area-filling factor of line-emitting regions in the molecular cloud will increase (Imanishi et al. 2007b). Practically, there can be a wide spread in a clump’s line opacity. Clumps which are initially optically thin for a certain molecular line under non-enhanced abundance can radiate stronger molecular line emission when the abundance of that molecule is enhanced. It is very likely that  $\text{HCN}$  and  $\text{HCO}^+$  emission line flux increases with increasing abundance in actual molecular clouds in galaxies.

emission lines probe the same spatial and dynamical gas components at the innermost northwestern torus.

The corresponding blueshifted emission components at the innermost southeastern torus, expected from (sub-)Keplerian rotation, are much weaker both for HCN J=3–2 and HCO<sup>+</sup> J=3–2 lines (Figure 3a,b). This is also the case for H<sub>2</sub>O maser emission (Greenhill et al. 1996; Greenhill & Gwinn 1997). In the spectra of the torus (14 pc × 7 pc) and western torus (7 pc × 7 pc) in Figure 8, an emission excess (compared with the single Gaussian fit) is seen at the redshifted part, at  $V \sim 1300\text{--}1500 \text{ km s}^{-1}$  ( $V_{\text{sys}} + [170\text{--}370] \text{ km s}^{-1}$ ) in both HCN J=3–2 and HCO<sup>+</sup> J=3–2. This is most likely originating in the dynamically decoupled, redshifted high velocity dense molecular line emission from the innermost northwestern torus (Figure 3a,b). A similarly strong excess emission at  $V \sim 760\text{--}960 \text{ km s}^{-1}$  ( $V_{\text{sys}} - [170\text{--}370] \text{ km s}^{-1}$ ) is not clearly seen in the spectra at the eastern and whole torus (Figure 8). This could be understood if the amount of blueshifted HCN, HCO<sup>+</sup>, and H<sub>2</sub>O molecules at the innermost southeastern torus is smaller than that of redshifted molecules at the innermost northwestern torus, because it seems very unlikely that all of these molecular emission lines at 22–260 GHz (1.2–14 mm) are strongly flux attenuated by dust extinction, free-free absorption, and/or line opacity (§4.1) only at the innermost southeastern side.

Figure 13 shows position velocity diagrams of HCN J=3–2 and HCO<sup>+</sup> J=3–2 lines along the position angle of PA = 115° east of north. This position angle is in between the innermost ( $\lesssim 0.7 \text{ pc}$ ) dense molecular line emission with PA  $\sim 135^\circ$  and outer torus (2–5 pc) emission with PA = 105–110° (Imanishi et al. 2018a). Redshifted HCN J=3–2 emission with  $V \sim 1300\text{--}1500 \text{ km s}^{-1}$  ( $V_{\text{sys}} + [170\text{--}370] \text{ km s}^{-1}$ ) is clearly detected at the innermost northwestern torus (right side of the SMBH in Figure 13a), while the corresponding blueshifted HCN J=3–2 emission with  $V \sim 760\text{--}960 \text{ km s}^{-1}$  ( $V_{\text{sys}} - [170\text{--}370] \text{ km s}^{-1}$ ) at the innermost southeastern torus is much less clear. This reinforces the above scenario that dense molecular gas distribution at the innermost torus, just outside the mass-accreting SMBH, is asymmetric in such a way that there is much more gas at the northwestern side than at the southeastern side.

Summarizing, we suggest that the spatial distribution of H<sub>2</sub>O, HCN, and HCO<sup>+</sup> at the innermost ( $\lesssim 1 \text{ pc}$ ) torus is asymmetric in that they are found in larger amounts on the northwestern side. The dynamics of these northwestern molecular emission follows almost Keplerian rotation at  $\lesssim 0.7 \text{ pc}$ .

#### 4.4. Dynamical properties of the torus

While the redshifted emission component at the northwestern torus roughly follows an almost-Keplerian rotation at the innermost part at  $\lesssim 0.7 \text{ pc}$ , it starts to deviate from that, rotating far below the Keplerian at  $\gtrsim 0.7 \text{ pc}$  (Figure 12). It was found that the outer part of the northwestern torus at 2–5 pc showed blueshifted dense molecular emission, contrary to the innermost redshifted emission (Imanishi et al. 2018a; Impellizzeri et al. 2019). We perform a detailed dynamical investigation of the dense molecular emission in the W- and E-torus separately, because the emission properties are highly asymmetric.

Figure 14 plots the peak velocity and velocity width of HCN J=3–2 and HCO<sup>+</sup> J=3–2 emission, based on the Gaussian fit of beam-sized spectra extracted at various distances from the central SMBH along PA = 115°. At 2–6 pc, the dense molecular emission is blueshifted and redshifted, with respect to the systemic, in the northwestern and southeastern torus, respectively (Figure 14a). These velocity patterns are the opposite of those at the innermost ( $\lesssim 0.7 \text{ pc}$ ) torus, both in the west and east, supporting the presence of counter-rotating dense molecular gas (Impellizzeri et al. 2019).



The suggested counter-rotating dense molecular gas can also naturally explain the positional shift of the highest velocity dispersion spot in the northwestern torus in the moment 2 map, relative to the innermost redshifted high-velocity ( $V \gtrsim 1300 \text{ km s}^{-1}$  or  $V_{\text{sys}} + [\gtrsim 170] \text{ km s}^{-1}$ ) line-emitting region; the former is located just outside the latter (Figure 3). This is also confirmed in Figures 14a and 14b. In a counter-rotating molecular gas, the highest velocity dispersion value can be observed at the border between the innermost redshifted and outer blueshifted components, owing to beam dilution and/or increased turbulence created through instability.

The implied rotation velocity of outer ( $\gtrsim 2 \text{ pc}$ ) torus dense molecular gas looks much slower than Keplerian motion governed by the central SMBH mass (Figure 14a), as seen in previously taken ALMA data (Garcia-Burillo et al. 2016; Imanishi et al. 2018a). The intrinsic rotation velocity can be larger than the observed one by a factor of  $1/\sin(i)$ , where  $i$  is an inclination angle ( $i = 90^\circ$  for an edge-on view). As described in §3, since NGC 1068 is a type-2 AGN where the central mass-accreting SMBH is believed to be obscured by a dusty molecular torus, it is very likely that the torus inclination is  $i \sim 90^\circ$  (edge-on), rather than  $i \sim 0^\circ$  (face-on). In fact, recent high-spatial-resolution ( $< 0''.1$ ) observations in the infrared–(sub)millimeter wavelength region have consistently supported a nearly edge-on ( $i > 60^\circ$ ) view of the NGC 1068 torus (Garcia-Burillo et al. 2019; Gravity Collaboration et al. 2020; Lopez-Rodriguez et al. 2020). Garcia-Burillo et al. (2016) estimated that the torus inclination is  $i \sim 90^\circ$  at the innermost part at  $\lesssim 1 \text{ pc}$ , but  $i = 34\text{--}66^\circ$  at the outer part at  $\gtrsim 2\text{--}4 \text{ pc}$ . Even adopting the small value of  $i = 34\text{--}66^\circ$ , the intrinsic rotation velocity can be higher than the observed one only by a factor of  $1/\sin(i) = 1.1\text{--}1.8$  and is still significantly slower than the Keplerian rotation.

Summarizing, based on our ALMA data, we prefer a scenario in which an outer ( $\gtrsim 2 \text{ pc}$ ) dense molecular gas is rotating slowly (much slower than Keplerian) and counter-rotating with respect to the innermost dense gas component. This slowly rotating outer ( $\gtrsim 2 \text{ pc}$ ) torus scenario is different from the argument of almost Keplerian rotation there by Impellizzeri et al. (2019).

#### 4.5. *Vibrationally excited dense molecular emission lines*

A luminous AGN can emit a strong mid-infrared ( $3\text{--}30 \mu\text{m}$ ) continuum due to AGN-heated hot ( $> 100 \text{ K}$ ) dust. HCN molecules can be vibrationally excited to the  $v_2=1$  level ( $> 1000 \text{ K}$ ) by absorbing mid-infrared  $\sim 14 \mu\text{m}$  photons (Aalto et al. 1995; Rangwala et al. 2011). In fact, an HCN  $v_2=1, l=1f$  (HCN-VIB) J=3–2 emission line was detected in several luminous buried AGNs, surrounded by a large column density of dense molecular gas (Sakamoto et al. 2010; Aalto et al. 2015a,b; Costagliola et al. 2015; Martin et al. 2016; Imanishi et al. 2016b). NGC 1068 contains a luminous AGN ( $L_{\text{AGN}} > 4 \times 10^{44} \text{ erg s}^{-1}$ ) (Bock et al. 2000; Gravity Collaboration et al. 2020), surrounded by Compton-thick ( $N_{\text{H}} > 10^{24} \text{ cm}^{-2}$ ) obscuring material (Koyama et al. 1989; Ueno et al. 1994; Matt et al. 1997; Bauer et al. 2015; Marinucci et al. 2016; Zaino et al. 2020). Hence, it is quite possible that the HCN-VIB J=3–2 emission line is strongly radiated in the NGC 1068 torus where dense molecular gas is illuminated by the AGN-origin mid-infrared  $\sim 14 \mu\text{m}$  photons. However, this HCN-VIB J=3–2 emission line has not been clearly detected in NGC 1068 at the systemic velocity ( $V_{\text{sys}} = 1130 \text{ km s}^{-1}$ ) in previously taken ALMA spectra (Imanishi et al. 2016a, 2018a).

In Figure 6b, an absorption feature is seen at  $V \sim 1400\text{--}1700 \text{ km s}^{-1}$  ( $V_{\text{sys}} + [270\text{--}570] \text{ km s}^{-1}$ ) in the HCO<sup>+</sup> J=3–2 line spectrum. If this originates in HCO<sup>+</sup> J=3–2 absorption, the redshifted  $\gtrsim 270 \text{ km s}^{-1}$  velocity seems too large for infalling gas, unless it is located very close to the central SMBH and is strongly affected by its gravitational force. In such close proximity to a luminous AGN, HCN abundance is expected to be higher than that of HCO<sup>+</sup>, owing to AGN radiation and/or

mechanical effects (§4.1), but we see no clear absorption signature at  $V \sim 1400\text{--}1700 \text{ km s}^{-1}$  ( $V_{\text{sys}} + [270\text{--}570] \text{ km s}^{-1}$ ) for plausibly more abundant HCN (Figure 6a). It seems unlikely that infalling  $\text{HCO}^+$  gas is the origin of the detected  $V \sim 1400\text{--}1700 \text{ km s}^{-1}$  absorption feature. The frequency of this absorption feature coincides with the HCN-VIB J=3–2 line at  $V_{\text{sys}} = 1130 \text{ km s}^{-1}$  (Figure 4a). We pursue this possibility. In fact, an HCN-VIB absorption feature at J=4–3 has recently been detected with ALMA in a nearby bright obscured AGN, NGC 1052 (Kameno et al. 2020). Applying a Gaussian fit to this absorption feature (velocity integrated flux =  $-130 \pm 32 \text{ mJy beam}^{-1} \text{ km s}^{-1}$ ) and adopting the continuum flux level of  $6.5 \text{ (mJy beam}^{-1})$  in data-a (Table 2), we obtain the absorption equivalent width to be  $EW \sim 2 \times 10^6 \text{ (cm s}^{-1})$ . We can convert this EW to the absorbing column density using the formula

$$EW = \frac{\lambda^3 A_{ul} g_u}{8\pi g_l} \times N \quad (3)$$

(Rybicki & Lightman 1979; Gonzalez-Alfonso et al. 2014), where EW is in units of ( $\text{cm s}^{-1}$ );  $\lambda$  is wavelength (in cm);  $A_{ul}$  is the Einstein A coefficient for spontaneous emission from the upper (u) level to the lower (l) level in units of ( $\text{s}^{-1}$ );  $g_u$  and  $g_l$  are the statistical weights ( $= 2J + 1$ ) at the upper and lower levels, respectively; and  $N$  is the column density in the lower energy level, in units of ( $\text{cm}^{-2}$ ). The  $A_{ul}$  value for HCN-VIB J=3–2 is  $7.3 \times 10^{-4} \text{ (s}^{-1})$  at Splatalogue (Müller et al. 2005). We obtain the column density of vibrationally excited HCN at J=2 to be  $N_{\text{HCN-VIB J=2}} \sim 3.5 \times 10^{13} \text{ cm}^{-2}$ . Even if we adopt an enhanced HCN-to- $\text{H}_2$  abundance ratio of  $\sim 10^{-8}$  (§4.1), we obtain the column density of  $\text{H}_2$  co-existing with vibrationally excited HCN to be as high as  $N_{\text{H}_2} \sim \text{a few} \times 10^{21} \text{ cm}^{-2}$ . This is a lower limit because vibrationally excited HCN can be populated at other J-transitions. If the central luminous AGN is surrounded by this column density of mid-infrared-pumped molecular gas in all torus directions, we may expect to detect the HCN-VIB line in *emission*. We thus search for this emission signature in our sensitive ALMA spectrum.

In the W-peak spectrum in Figure 4c, at the lower frequency side of the  $\text{HCO}^+$  J=3–2 emission line, we see a distinct emission line at  $\nu_{\text{obs}} \sim 266.0 \text{ GHz}$  (denoted as “HCN-VIB J=3–2 (red)”), which corresponds to the HCN-VIB J=3–2 line at  $V \sim 1340 \text{ km s}^{-1}$  ( $V_{\text{sys}} + 210 \text{ km s}^{-1}$ ). A Gaussian fit to this line is shown in Figure 5e. The estimated peak velocity and velocity-integrated emission line flux are  $1339 \pm 7 \text{ (km s}^{-1})$  and  $0.041 \pm 0.009 \text{ (Jy km s}^{-1})$ , respectively (Table 3). Using Equations (1) and (2), the HCN-VIB J=3–2 emission line luminosity is estimated to be  $L_{\text{HCN-VIB J=3-2}} \sim 2.2 \text{ (} L_{\odot})$  or  $L'_{\text{HCN-VIB J=3-2}} \sim 3.6 \times 10^3 \text{ (K km s}^{-1} \text{ pc}^2)$ . Since the HCN-VIB J=3–2 emission line is detected clearly only in the beam-sized W-peak spectrum, we use the luminosity as that from the NGC 1068 torus. The HCN-VIB J=3–2 emission line luminosity is about two orders of magnitude smaller than that of the HCN J=3–2 emission line from the whole torus region (§4.2). This  $\sim 1\%$  HCN-VIB-to-HCN luminosity ratio is much smaller than several HCN-VIB-line-detected buried AGNs (and such candidates) in nearby luminous infrared galaxies, where the HCN-VIB-to-HCN J=3–2 luminosity ratios are  $>5\%$  (Sakamoto et al. 2010; Aalto et al. 2015a,b; Costagliola et al. 2015; Martin et al. 2016; Imanishi et al. 2016b).

In NGC 1068, since no directly transmitted X-ray emission is seen even at  $\sim 60\text{--}100 \text{ keV}$  (Matt et al. 1997; Bauer et al. 2015; Marinucci et al. 2016), the absorbing column density toward the X-ray emitting region around the central luminous AGN is likely to be as high as  $N_{\text{H}} \gtrsim 10^{25} \text{ cm}^{-2}$  (i.e., heavily Compton thick). If the central luminous AGN is surrounded by material with this high column density in virtually all directions, HCN-VIB J=3–2 emission line luminosity can be high, relative to the



HCN J=3–2 emission line luminosity, through the greenhouse effect (Gonzalez-Alfonso & Sakamoto 2019). It may be that the volume- (and area-) filling factor of dense absorbing gas clumps in the NGC 1068 torus is substantially smaller than the HCN-VIB-line-detected infrared luminous galaxies, which are mostly major mergers. The physical scale of the mid-infrared hot dust-emitting region around a luminous AGN (larger than the innermost torus dust sublimation radius;  $\gtrsim 0.1$  pc for  $L_{\text{AGN}} > 4 \times 10^{44}$  [erg s<sup>-1</sup>] (Barvainis 1987)) is much larger than that of the X-ray emitting region ( $\lesssim 10$  Schwarzschild radius or  $\lesssim 10^{-5}$  pc for the  $1 \times 10^7 M_{\odot}$  SMBH). Thus, it is possible that the X-ray emission is completely blocked by foreground dense clumps, while a large fraction of the mid-infrared emission can escape without being absorbed by the surrounding obscuring material. This could explain the observed low HCN-VIB-to-HCN J=3–2 emission line luminosity ratio in the NGC 1068 torus. In fact, the mid-infrared 3–13  $\mu\text{m}$  spectra toward the NGC 1068 nucleus, excluding the bright ring-shaped ( $\sim 10$ – $15''$  radius) starburst ring emission, show modestly strong 3.4  $\mu\text{m}$  carbonaceous dust and 9.7  $\mu\text{m}$  silicate dust absorption features (Roche et al. 1991; Imanishi et al. 1997; Rhee & Larkin 2006; Mason et al. 2006; Geballe et al. 2009). However, their optical depths are much smaller than several buried AGNs, whose mid-infrared continua are thought to be almost fully blocked by the foreground obscuring dust (e.g., Imanishi & Dudley 2000; Imanishi et al. 2006a; Levenson et al. 2007; Spoon et al. 2007; Imanishi et al. 2007a, 2008, 2010), suggesting a large fraction of leaked mid-infrared continuum emission through the NGC 1068 torus.

It is reasonable that the HCN-VIB J=3–2 emission is detected as the redshifted ( $V \gtrsim 1300$  km s<sup>-1</sup> or  $V_{\text{sys}} + [\gtrsim 170]$  km s<sup>-1</sup>) component in the beam-sized W-peak spectrum (Figure 4c) for two reasons. First, the amount of HCN is larger at the redshifted innermost northwestern torus than it is at the blueshifted innermost southeastern torus (§4.3). Secondly, there should be plenty of mid-infrared  $\sim 14$   $\mu\text{m}$  photons that were emitted from AGN-heated hot dust grains. Both of these conditions can naturally produce strong HCN-VIB J=3–2 emission from the redshifted HCN gas at the innermost northwestern torus, which is covered in the beam-sized W-peak spectrum, but not in the beam-sized E-peak spectrum. We create a moment 0 map of HCN-VIB J=3–2 line, by integrating signals of redshifted components ( $V = 1170$ – $1430$  km s<sup>-1</sup> or  $V_{\text{sys}} + [40$ – $300]$  km s<sup>-1</sup>), which is shown in Figure 15. The HCN-VIB J=3–2 emission line is detected with  $\sim 4.8\sigma$  at the northwestern side of the C-peak (close to the W-peak), supporting the scenario in which the HCN-VIB J=3–2 emission comes from the redshifted dense molecular gas at the innermost northwestern torus.

No clear absorption feature is seen at the expected frequency of HCO<sup>+</sup>-VIB J=3–2 line for  $V_{\text{sys}} = 1130$  km s<sup>-1</sup> in the spectrum toward the C-peak (Figure 4a). In the W-peak spectrum (Figure 4c), some emission line signature is seen at the frequency of the HCO<sup>+</sup>-VIB J=3–2 line with  $V \sim 1340$  km s<sup>-1</sup> ( $V_{\text{sys}} + 210$  km s<sup>-1</sup>; denoted as “HCO<sup>+</sup>-VIB J=3–2 (red)”). If this line identification is correct, this may be the first detection of an HCO<sup>+</sup>-VIB J=3–2 line in *emission* in an external galaxy. Only HCO<sup>+</sup>-VIB line detection in *absorption* has been reported at J=4–3 in an obscured AGN (Kameno et al. 2020). HCO<sup>+</sup> can be vibrationally excited to the  $v_2=1$  level by absorbing mid-infrared  $\sim 12$   $\mu\text{m}$  photons. Since there is plenty of AGN-heated hot dust at the innermost northwestern torus, strong HCO<sup>+</sup>-VIB J=3–2 emission may be produced. However, our Gaussian fit of this possible emission line provides detection significance of  $< 3\sigma$ . Additionally, the observed peak frequency of this possible emission line corresponds also to HOC<sup>+</sup> J=3–2 ( $\nu_{\text{rest}} = 268.451$  GHz) at  $V_{\text{sys}} \sim 1130$  km s<sup>-1</sup> (Figure 4c). This HOC<sup>+</sup> J=3–2 emission line can be strong in molecular gas illuminated by strong X-ray radiation, such as an AGN torus (Usero et al. 2004; Qiu et al. 2020), and

was actually detected in a few luminous obscured AGNs and such candidates (Aalto et al. 2015a,b; Imanishi et al. 2016b; Aladro et al. 2018). The HCO<sup>+</sup>-VIB J=3–2 emission line is still elusive, even in the nearby luminous AGN, NGC 1068. The detection of HCN-VIB line and no clear detection of HCO<sup>+</sup> line are consistent with the enhanced HCN abundance scenario in the torus (discussed in §4.1).

HNC can also be vibrationally excited to the  $v_2=1$  level by absorbing mid-infrared  $\sim 21.5 \mu\text{m}$  photons, but we see neither a clear emission nor an absorption signature of the HNC-VIB J=3–2 line in torus spectra (Figure 4g,h,i). The HNC J=3–2 emission from the torus is much weaker than HCN J=3–2 and HCO<sup>+</sup> J=3–2 emission (Figure 4), suggesting a low HNC abundance there. The temperature of molecular gas and dust in the torus in the vicinity of a luminous AGN is higher than that in the general inter-stellar medium in the host galaxy. Since an HNC abundance is known to decrease in Galactic high-temperature molecular clouds around active regions (Schilke et al. 1992; Hirota et al. 1998; Graninger et al. 2014), this may be the case also for the NGC 1068 torus. Under low HNC abundance, the HNC-VIB J=3–2 emission line can be weak.

Summarizing, HCN-VIB J=3–2 line signatures are seen in absorption in the beam-sized spectrum toward the C-peak and in emission originating from the redshifted molecular gas at the innermost northwestern torus (detected in the beam-sized W-peak spectrum). The observed small HCN-VIB-to-HCN J=3–2 emission line flux ratio suggests that the NGC 1068 torus is highly clumpy, and a large fraction of mid-infrared  $\sim 14 \mu\text{m}$  photons emitted from AGN-heated hot dust grains escape without being absorbed by HCN molecules in the torus. Absorption and emission signatures of the HCO<sup>+</sup>-VIB J=3–2 and HNC-VIB J=3–2 lines are much less clear.

#### 4.6. *Molecular emission in the eastern torus*

Although velocity-integrated emission line fluxes of both HCN J=3–2 and HCO<sup>+</sup> J=3–2 are significantly higher at the W-peak than at the E-peak in moment 0 maps (Figure 2a,b) and beam-sized spectra (Table 3, column 9), those within the  $7 \text{ pc} \times 7 \text{ pc}$  ( $0''.1 \times 0''.1$ ) region are higher in the E-torus than in the W-torus (Table 4, column 6), suggesting that a larger amount of spatially extended low-surface-brightness molecular line emission outside the compact ( $\lesssim 3 \text{ pc}$ ) main torus is present in the E-torus. In fact, in the moment 0 and 1 maps of HCN J=3–2, we recognize spatially extended, low-surface-brightness emission outside the main E-torus as far east as R.A. =  $02^{\text{h}} 42^{\text{m}} 40.714^{\text{s}}$  (Figure 2a,c). Imanishi et al. (2016a, 2018a) also marginally detected signatures of bridging HCN J=3–2 emission between the E-torus and massive molecular clouds in the host galaxy, at the eastern side of the E-torus. Müller Sanchez et al. (2009) also argued the presence of molecular gas falling toward the E-torus from the eastern side, based on near-infrared  $2.2 \mu\text{m}$  observations of very hot ( $>1000 \text{ K}$ ) molecular gas (but see Barbosa et al. (2014); May & Steiner (2017); Garcia-Burillo et al. (2019)).

Molecular gas in the host galaxy at  $\sim 50\text{--}150 \text{ pc}$  on the eastern side of the torus is located on a far side (Garcia-Burillo et al. 2019) and shows blueshifted ( $V \sim 1000\text{--}1100 \text{ km s}^{-1}$  or  $V_{\text{sys}} - [30\text{--}130] \text{ km s}^{-1}$ ) emission (Schinnerer et al. 2000; Krips et al. 2011; Garcia-Burillo et al. 2014, 2016; Imanishi et al. 2016a, 2018a; Garcia-Burillo et al. 2019). The velocity of the dense molecular line emission just on the eastern side of the E-torus ( $V \sim 1100\text{--}1130 \text{ km s}^{-1}$  or  $V_{\text{sys}} - [0\text{--}30] \text{ km s}^{-1}$  at  $\sim 5 \text{ pc}$  from the SMBH; R.A. =  $02^{\text{h}} 42^{\text{m}} 40.714^{\text{s}}$  shown as a black upward arrow in Figure 2c) is between that of the eastern host galaxy ( $V \sim 1000\text{--}1100 \text{ km s}^{-1}$  or  $V_{\text{sys}} - [30\text{--}130] \text{ km s}^{-1}$ ) and that of the redshifted, outer portion of the compact main E-torus ( $V \sim 1140\text{--}1150 \text{ km s}^{-1}$  or  $V_{\text{sys}} + [10\text{--}20] \text{ km s}^{-1}$  at  $2\text{--}3 \text{ pc}$  on the eastern side of the SMBH; R.A. =  $02^{\text{h}} 42^{\text{m}} 40.712^{\text{s}}$  indicated with the

leftmost red downward arrow in Figure 2c). Figure 16 illustrates the above geometry and dynamics. Velocity at the southeastern torus along PA = 115° also displays a sudden change at ~7 pc from inner redshifted motion to outer blueshifted motion (Figure 14). This bridging emission at 5–7 pc east of the SMBH could be related to molecular gas being transported from the eastern host galaxy (far side) to the E-torus (front side) and may contribute to an increase in the dense molecular line flux in the 7 pc × 7 pc area-integrated E-torus spectrum.

#### 4.7. Outflowing dense molecular gas

We now investigate the signatures of molecular outflow from the NGC 1068 nucleus, whose detection was reported in several papers (Garcia-Burillo et al. 2014; Gallimore et al. 2016; Impellizzeri et al. 2019; Garcia-Burillo et al. 2019). Searches for massive molecular outflows have usually targeted the presence of a very broad emission line wing component, in addition to a main molecular emission component determined by galaxy dynamics (e.g., Maiolino et al. 2012; Cicone et al. 2014; Garcia-Burillo et al. 2015; Imanishi et al. 2017; Pereira-Santaella et al. 2018; Lutz et al. 2020). In the molecular line spectra from the torus (Figure 8), besides the redshifted emission excess most likely originating from the redshifted high velocity component at the innermost northwestern torus (§4.3), a broad emission component is not clearly detected.

We instead investigate the beam-sized spectra at the C-peak, which show absorption features. The velocity profile of the HCN J=3–2 line in Figure 6a shows a broad absorption tail at the blueshifted side ( $V = 700\text{--}1100 \text{ km s}^{-1}$  or  $V_{\text{sys}} - [30\text{--}430] \text{ km s}^{-1}$ ). This can be explained by outflow activity (Impellizzeri et al. 2019). A similar blueshifted absorption tail is much weaker in the HCO<sup>+</sup> J=3–2 line spectrum in Figure 6b. Since the beam-size ( $\sim 0\prime.02 \times 0\prime.02$ ) is not sufficiently smaller than the separation between the central SMBH position and the innermost dense molecular emission from the E- and W-torus, the beam-sized spectra at the C-peak (Figure 6) can be contaminated by emission from the innermost torus. We attempt to correct for this contamination by averaging the spectra at the 0<sup>′</sup>02 northeast and southwest sides of the SMBH (i.e., perpendicular to the northwest- and southeast-oriented innermost torus emission) and subtracting the average from the observed spectrum at the C-peak, following Impellizzeri et al. (2019). The corrected HCN J=3–2 and HCO<sup>+</sup> J=3–2 line spectra at the C-peak are displayed in Figure 6 (red dotted line). For HCN J=3–2, the peak absorption depth in the corrected spectrum is slightly smaller than that estimated by Impellizzeri et al. (2019), but this difference can be caused by different beam patterns resulting in different correction degrees of the contamination. What is more important is that the blueshifted absorption tail of HCN J=3–2 becomes clearer, and that of HCO<sup>+</sup> J=3–2 is also seen, supporting the presence of dense molecular outflow coming toward us from the ~260-GHz-continuum-emission-peak position around the mass-accreting SMBH. We interpret that this outflow is still confined to the compact nuclear region of NGC 1068, because an enhanced HCN abundance affected by a luminous AGN (§4.1) can naturally explain an outflow feature in HCN J=3–2 that is stronger than in HCO<sup>+</sup> J=3–2. No signature of an outflow-origin blueshifted absorption tail is seen in HNC J=3–2 (Figure 4g), as expected from low HNC abundance in molecular gas in the vicinity of the AGN (§4.5).

We apply a Gaussian fit to the broad blueshifted HCN J=3–2 absorption wing in the raw beam-sized spectrum at the C-peak in Figure 6a, and obtain the central velocity of  $991 \pm 27 \text{ (km s}^{-1}\text{)}$ , FWHM =  $295 \pm 45 \text{ (km s}^{-1}\text{)}$ , peak absorption dip of  $-0.51 \pm 0.08 \text{ (mJy beam}^{-1}\text{)}$ , and velocity integrated flux of  $-162 \pm 35 \text{ (mJy beam}^{-1} \text{ km s}^{-1}\text{)}$ . Adopting the continuum flux of  $6.5 \text{ (mJy beam}^{-1}\text{)}$  (Table 2), we obtain an absorption dip of ~8% ( $\tau \sim 0.08$ ; i.e., optically thin) and absorption equivalent

width of  $EW_{\text{HCN}32 \text{ outflow}} = 2.5 \pm 0.5 \times 10^6 \text{ (cm s}^{-1}\text{)}$ . Using Equation (3), we estimate the HCN J=2 column density of the outflow to be  $3.7 \pm 0.8 \times 10^{13} \text{ (cm}^{-2}\text{)}$ , where  $A_{\text{ul}} = 8.4 \times 10^{-4} \text{ (s}^{-1}\text{)}$  is adopted for HCN J=3–2 (Müller et al. 2005). If these outflowing HCN molecules spatially distribute in the beam size ( $0''.019 \times 0''.017$  or  $1.3 \text{ pc} \times 1.2 \text{ pc}$ ; Table 2), the derived column density corresponds to  $(44 \pm 10) \times 10^{49}$  HCN molecules, or even larger if we take into account HCN at other J-transitions. Assuming a high HCN-to- $\text{H}_2$  abundance ratio of  $10^{-8}$  (§4.1) because the outflow is supposed to be confined to the nuclear region, we obtain the outflowing dense  $\text{H}_2$  mass to be  $M_{\text{outflow}} \gtrsim 75 M_{\odot}$ . This mass corresponds to outflow within the  $1.3 \text{ pc} \times 1.2 \text{ pc}$  area in front of the  $\sim 260\text{-GHz}$ -continuum-emitting region. If the outflowing gas is clumpy and the area-filling factor of clumps, which show the absorption line, is 50% (10%), each clump should show an absorption dip of  $\sim 16\%$  ( $\sim 80\%$ ) or  $\tau \sim 0.17$  ( $\tau \sim 1.6$ ), respectively, where continuum flux attenuation by dust extinction is neglected at  $\sim 260 \text{ GHz}$  ( $\sim 1.2 \text{ mm}$ ). For a very small area-filling factor ( $\ll 100\%$ ), the clump will be in an optically thick non-linear regime for the absorption line strength, so the outflow mass will increase. Furthermore, if the outflow is spatially more extended in the transverse direction than the  $1.3 \text{ pc} \times 1.2 \text{ pc}$  area, the actual outflow mass will be even larger. Adopting the outflow velocity of  $V_{\text{outflow}} \sim 140 \text{ (km s}^{-1}\text{)}$  ( $V_{\text{sys}} - 991 \text{ km s}^{-1}$ ), the outflow energy is estimated to be  $E_{\text{outflow}} \gtrsim 1.4 \times 10^{42} \text{ (J)}$ .

Such an energetic outflow can disturb the dynamics of the innermost torus molecular gas and could reproduce a dynamically decoupled innermost ( $\lesssim 0.7 \text{ pc}$ ) emission component from the outer ( $\gtrsim 2 \text{ pc}$ ) torus emission, as observed in Figure 3a,b. In fact, Garcia-Burillo et al. (2019) prefer an outflow scenario, rather than the counter-rotating molecular gas scenario, to explain their obtained  $\gtrsim 0''.03$ -resolution molecular gas dynamics of the NGC 1068 torus. However, the dynamical similarity between the innermost HCN J=3–2 and almost-Keplerian rotating  $\text{H}_2\text{O}$  maser emission (§4.3) leads us to prefer the counter-rotating molecular gas scenario as the origin of the redshifted dense molecular emission from the innermost northwestern torus, because there is no strong reason why the dynamical properties of the  $\text{H}_2\text{O}$  maser rotating disk and outflowing molecular gas agree.

#### 4.8. Schematic picture of the NGC 1068 torus

After considering all observational results, we provide a schematic picture of dense molecular gas in the NGC 1068 torus in Figure 17. There are two components of dense molecular gas that are counter-rotating (i.e., an innermost [ $\lesssim 0.7 \text{ pc}$ ] component characterized by almost-Keplerian rotation and an outer [ $\gtrsim 2 \text{ pc}$ ] component characterized by slow rotation [much slower than Keplerian rotation]). Outflowing dense molecular gas from the central mass-accreting SMBH in our direction and redshifted high velocity ( $V = 1300\text{--}1500 \text{ km s}^{-1}$  or  $V_{\text{sys}} + [170\text{--}370] \text{ km s}^{-1}$ ) HCN-VIB J=3–2, HCN J=3–2, and  $\text{HCO}^+$  J=3–2 emission originating in the innermost northwestern torus are present.

Counter-rotating dense molecular gas in the compact torus can be quickly relaxed dynamically (Garcia-Burillo et al. 2019). To produce such a transient, short-time-scale counter-rotation within the  $\lesssim 7 \text{ pc}$  torus scale, some external force seems required. We propose a simple scenario that a compact massive gas clump fell into the pre-existing torus and collided with the western torus from the far side. Such an infalling gas clump may originate in minor galaxy merger (Furuya & Taniguchi 2016; Tanaka et al. 2017) or streaming motion (Müller Sanchez et al. 2009). The western part of the pre-existing torus had been redshifted before the collision, as seen in the innermost ( $\lesssim 0.7 \text{ pc}$ )  $\text{H}_2\text{O}$  maser dynamics. The collision changed the dynamics of the bulk of the western torus to the blueshifted motion. The observed rotation, much slower than the Keplerian at  $\gtrsim 2 \text{ pc}$ , could be explained in this transient phase. Dense molecular gas at the innermost ( $\lesssim 0.7 \text{ pc}$ ) northwestern



torus could remain redshifted if it is gravitationally affected more strongly by the central SMBH mass than by the outer collision-induced turbulence. Such a colliding clump could make significant turbulence in the W-torus and explain the fact that the observed dense molecular emission line widths are larger in the W-torus than in the E-torus (Figure 8 and Table 4). This may also be related to the asymmetric dense molecular gas distribution at the innermost torus, where there is a larger amount of gas on the W-torus side (§4.3).

In order for this scenario to work quantitatively, the angular momentum of the colliding compact massive gas clump must be as large as that of the pre-existing torus. Since the pre-existing torus mass can be as high as  $\gtrsim$ a few  $\times 10^5 M_\odot$  (§4.2), the clump should be as massive as  $\gtrsim$ a few  $\times 10^5 M_\odot$ , in the case that the infalling velocity is comparable to the pre-collisional torus rotation velocity at the impact point. In our Galaxy and nearby galaxies, the bulk of giant molecular clouds (GMCs) are as massive as  $\gtrsim$ a few  $\times 10^5 M_\odot$  (Solomon et al. 1987; Fukui & Kawamura 2010). Recent ALMA high-spatial-resolution observations have revealed the presence of a very compact, massive GMC ( $>5 \times 10^6 M_\odot$  within  $<25$  pc) (Johnson et al. 2015). Assuming the same gas volume number density, a GMC with  $\gtrsim$ a few  $\times 10^5 M_\odot$  can be as small as  $\lesssim 8$  pc. If we adopt the relation between SMBH mass and bulge velocity dispersion established in the local universe (e.g., Ferrarese & Merritt 2000; Kormendy & Ho 2013), the SMBH mass of  $\sim 1 \times 10^7 M_\odot$  in NGC 1068 corresponds to the bulge velocity dispersion of  $\sim 100$  km s<sup>-1</sup>. On the other hand, the Keplerian velocity at  $\sim 5$  pc for  $M_{\text{SMBH}} \sim 1 \times 10^7 M_\odot$  is  $\sim 90$  km s<sup>-1</sup>. Thus, in terms of angular momentum, it is possible that the collision of a compact, highly dense, massive GMC with mass of  $\gtrsim$ a few  $\times 10^5 M_\odot$  and infalling velocity of  $\sim 100$  km s<sup>-1</sup> changed the rotation direction of the pre-existing, almost-Keplerian rotating torus at a  $\gtrsim 2$ -pc scale on the western side.

In a standard torus model, without invoking an external turbulence, velocity dispersion of only  $<20$  km s<sup>-1</sup> can be produced at  $\lesssim 7$  pc scale (Kawakatu et al. 2020). In the HCN J=3–2 and HCO<sup>+</sup> J=3–2 moment 2 maps (Figure 3c,d), the highest velocity dispersion value in the W-torus is  $\gtrsim 100$  km s<sup>-1</sup>. Although the border of the counter-rotating molecular gas could create an apparently large velocity dispersion due to beam dilution (§4.4), the fact that the observed HCN-to-HCO<sup>+</sup> J=3–2 flux ratio is higher at the W-peak than at the E-peak (Table 3, Figure 11) strongly suggests that the intrinsic turbulence is also higher at the W-peak (§4.1). It is possible that the GMC collision contributes to the increased turbulence there. The HCN J=3–2 and HCO<sup>+</sup> J=3–2 emission line flux in the beam-sized spectrum at the highly turbulent W-peak is  $0.45 \pm 0.04$  and  $0.30 \pm 0.04$  (Jy km s<sup>-1</sup>), respectively (Table 3, column 9). Using the same conversion as applied in §4.2, we obtain dense molecular mass close to the highly turbulent W-peak to be  $\sim 10^5 M_\odot$ , where the factor of 4–5 HCN overabundance is taken into account. If a GMC with mass of  $\gtrsim$ a few  $\times 10^5 M_\odot$  infalls to the W-torus with  $\sim 100$  km s<sup>-1</sup> velocity, the observed turbulence close to the W-peak could be explained energetically.

Once the collision-induced strong turbulence with  $\sigma \gtrsim 40$  km s<sup>-1</sup> happens in the W-torus at  $\sim 2$ -pc scale (Figures 3c,d, 14b), the turbulence can propagate to the E-torus with a timescale of  $\sim 0.1$  Myr ( $= \pi \times 2$  [pc] /  $\gtrsim 40$  [km s<sup>-1</sup>]), possibly explaining the observed counter-rotation in the E-torus as well. Forthcoming papers will present detailed numerical simulation results of the collision scenario (Wada et al. 2020, in preparation) as well as more detailed dynamical properties of dense molecular gas in the torus region (Nguyen et al. 2020, in preparation).

Our very-high-spatial-resolution ( $\sim 0''.02$ ) ALMA data have revealed very interesting and complicated dense molecular gas properties in the torus of the nearby well-studied type-2 AGN, NGC 1068. In a classical torus model, a simple, almost Keplerian rotation is assumed unless some turbulence is added, because molecular viscosity is too small to significantly extract the angular momentum of the torus in a short timescale. The torus is a structure where a large amount of dense molecular gas distributes in a compact area, outside an accretion disk around a central SMBH. Angular momentum removal of molecular gas in the torus can realize mass transport into the accretion disk and ignite AGN activity. The counter-rotating molecular torus is one way to achieve this (Impellizzeri et al. 2019) and may be the origin of the observed luminous AGN activity in NGC 1068 ( $L_{\text{AGN}} > 4 \times 10^{44} \text{ erg s}^{-1}$ ) (Bock et al. 2000; Gravity Collaboration et al. 2020). Future ALMA very-high-spatial-resolution molecular line observations of NGC 1068 and other nearby AGNs will further improve our understanding of the torus and its relation to luminous AGN activity in our universe.

## 5. SUMMARY

We have conducted ALMA very-high-spatial-resolution ( $\sim 0''.02$  or  $\sim 1.4 \text{ pc}$ ) observations of the nucleus of the nearby ( $\sim 14 \text{ Mpc}$ ) well-studied type-2 AGN, NGC 1068, at HCN, HCO<sup>+</sup>, and HNC J=3–2 lines, as well as at their <sup>13</sup>C isotopologue and vibrationally excited lines. These lines are suitable to observationally constrain the morphological/dynamical/chemical/physical properties of the dense molecular gas which is believed to be abundant in the putative torus around a mass-accreting SMBH. We found the following main results.

1. We confirmed almost east-west-oriented HCN J=3–2 and HCO<sup>+</sup> J=3–2 emission both morphologically and dynamically, as expected for the torus in NGC 1068. The primary bright emission comes from a  $\lesssim 3 \text{ pc}$  region, with the western side being significantly brighter than the eastern side. Low-surface-brightness dense molecular line emission is also seen outside the compact main torus component, out to  $\sim 7 \text{ pc}$ , roughly along the east-west direction. The total dense molecular mass within a  $14 \text{ pc}$  (east-west)  $\times 7 \text{ pc}$  (north-south) torus region is estimated to be  $M_{\text{torus}} = 0.4\text{--}1.0 \times 10^6 M_{\odot}$ , which is substantially smaller than the central SMBH mass with  $M_{\text{SMBH}} \sim 1 \times 10^7 M_{\odot}$ .
2. An outer torus at  $\gtrsim 2 \text{ pc}$  is blueshifted in the western part and redshifted in the eastern part, as previously seen (Imanishi et al. 2018a). However, the innermost torus at  $\lesssim 1 \text{ pc}$  is redshifted in the western part and blueshifted in the eastern part, the opposite of the outer torus, in both the HCN J=3–2 and HCO<sup>+</sup> J=3–2 lines. The dense molecular gas in the torus appears counter-rotating between the innermost and outer parts.
3. A redshifted high-velocity ( $V \sim 1300\text{--}1500 \text{ km s}^{-1}$  or  $V_{\text{sys}} + [170\text{--}370] \text{ km s}^{-1}$ ) emission component is seen at the innermost northwestern torus, both in the HCN J=3–2 and HCO<sup>+</sup> J=3–2 lines. The velocity of this component at  $\lesssim 0.7 \text{ pc}$  is comparable to that of a VLBI-detected, almost-Keplerian rotating  $\sim 22 \text{ GHz}$  H<sub>2</sub>O maser emission disk at the northwestern side of the central mass-accreting SMBH, suggesting that we are probing the same spatial and dynamical component there. The redshifted HCN J=3–2 and HCO<sup>+</sup> J=3–2 emission components are much brighter than the corresponding blueshifted components at the southeastern side, as seen in the H<sub>2</sub>O maser emission. It is suggested that dense molecular gas spatial distribution at the innermost torus is not symmetric in that the amount of gas is larger on the northwestern side than the southeastern side.



4. The western compact ( $\lesssim 3$  pc) main torus displays a larger velocity dispersion than the eastern main torus. The maximum velocity dispersion spot in the western torus is just outside the innermost redshifted high velocity component. This positional shift can also be explained by counter-rotating dense molecular gas because the velocity dispersion can be very large at the border of counter-rotating components owing to beam dilution and/or actual high turbulence caused by instability.
5. The HCN J=3–2 line in the spectrum toward the  $\sim 260$  GHz continuum emission peak displays a broad absorption wing at the blueshifted side of the systemic velocity ( $V_{\text{sys}} = 1130 \text{ km s}^{-1}$ ), which was interpreted to be resulting from dense molecular outflow. This blueshifted broad absorption signature is stronger in HCN J=3–2 than  $\text{HCO}^+$  J=3–2.
6. The vibrationally excited ( $v_2=1, l=1f$ ) HCN J=3–2 line (HCN-VIB) is detected in absorption in the spectrum toward the continuum peak and in redshifted ( $V \sim 1340 \text{ km s}^{-1}$  or  $V_{\text{sys}} + 210 \text{ km s}^{-1}$ ) emission at the innermost northwestern torus. The HCN-VIB-to-HCN J=3–2 emission line flux ratio is significantly smaller than those of other buried AGNs with detected HCN-VIB J=3–2 emission lines, possibly because of small volume- and area-filling factors of dense molecular clumps in the NGC 1068 torus.
7. The observed flux of HCN J=3–2 emission is systematically higher than that of  $\text{HCO}^+$  J=3–2 emission in the torus within a  $\sim 7$ -pc scale from the central SMBH. We attribute this to higher abundance of HCN than  $\text{HCO}^+$  in the torus region around a luminous AGN. Based on the isotopologue  $\text{H}^{13}\text{CN}$  J=3–2 and  $\text{H}^{13}\text{CO}^+$  J=3–2 absorption strengths in the spectrum toward the continuum peak, we derive a factor of  $>3$  higher abundance of HCN than  $\text{HCO}^+$ . This enhanced-HCN-abundance scenario is supported by various other observational results, including (1) higher HCN-to- $\text{HCO}^+$  J=3–2 emission line flux ratio in the more turbulent western compact main torus, (2) wider spatial distribution of significantly detected line emission in the torus region for HCN J=3–2 than for  $\text{HCO}^+$  J=3–2, despite a factor of  $\sim 5$  larger critical density for the former, (3) larger torus mass estimated from HCN than  $\text{HCO}^+$ , (4) stronger emission from the innermost northwestern torus and absorption toward the continuum peak for HCN-VIB J=3–2 than for  $\text{HCO}^+$ -VIB J=3–2. Radiative and/or mechanical effects of a luminous AGN may enhance HCN abundance more than  $\text{HCO}^+$  in the torus molecular gas.
8. An area-integrated ( $\sim 7$  pc) spectra demonstrated that molecular emission in the western torus shows a wider line profile. Together with the suggested counter-rotation of dense molecular gas in the torus, we conjecture that some external turbulence happened in the western torus, which may be related to the observed high AGN luminosity in NGC 1068, because angular momentum in the torus can be removed efficiently and mass accretion onto the central SMBH could be enhanced.

Our high-spatial-resolution ALMA data revealed that dense molecular gas properties in the torus in the nearby well-studied AGN, NGC 1068, are much more complex than the simple axi-symmetric, almost-Keplerian rotating torus picture. Further ALMA very-high-spatial-resolution observations of NGC 1068 and other nearby AGNs may help discover more interesting torus features and obtain a clearer view about the role of the dusty molecular torus in AGNs.

We thank Dr. Kazuya Saigo for his support to analyze ALMA data, and the anonymous referee for his/her valuable comment which helped significantly improve the clarity of this manuscript. This paper makes use of the following ALMA data: ADS/JAO.ALMA#2018.1.00037.S, #2017.1.01666.S, #2016.1.00052.S, and #2013.0.00188.S. ALMA is a partnership of ESO (representing its member states), NSF (USA) and NINS (Japan), together with NRC (Canada) and NSC and ASIAA (Taiwan), in cooperation with the Republic of Chile. The Joint ALMA Observatory is operated by ESO, AUI/NRAO and NAOJ. Data analysis was in part carried out on the open use data analysis computer system at the Astronomy Data Center, ADC, of the National Astronomical Observatory of Japan. This research has made use of NASA's Astrophysics Data System and the NASA/IPAC Extragalactic Database (NED) which is operated by the Jet Propulsion Laboratory, California Institute of Technology, under contract with the National Aeronautics and Space Administration.

*Facilities:* ALMA

## APPENDIX

### A. ALMA CYCLES 6 AND 5 DATA COMBINATION FOR HCN J=3–2 LINE

Impellizzeri et al. (2019) presented the results of ALMA Cycle 5  $\sim 0''.02$ -resolution HCN J=3–2 line observations of NGC 1068 (2017.1.01666.S). We combined our Cycle 6 and their Cycle 5 data, after excluding their short baseline (44–83 m) data, in order not to degrade the image size of the final data product. Figure 18 displays moment 0, 1, and 2 maps and a position velocity diagram of the HCN J=3–2 line for the combined data. Beam-sized spectra at the E-, W-, and C-peaks are shown in Figure 19. The main features detected in our Cycle 6 data in Figures 2, 3, 5, 6, and 13 are well reproduced in the combined data.

### B. COMPARISON WITH PREVIOUSLY TAKEN DATA FOR THE TORUS EMISSION

HCN J=3–2 and HCO<sup>+</sup> J=3–2 emission lines were significantly detected in previously taken (Cycles 4 and 2) lower-spatial-resolution ( $\gtrsim 0''.04$ ) data at the compact ( $< 10$  pc) torus (Imanishi et al. 2016a, 2018a). Figure 20 compares HCN J=3–2 and HCO<sup>+</sup> J=3–2 emission line profiles from the torus measured in a  $0''.15$ - or  $\sim 10$ -pc radius circular aperture, taken in Cycle 6 data, Cycle 4 data with long baseline only, and Cycles 4 and 2 combined data including both long and short baselines (Imanishi et al. 2018a). Emission profiles of both lines are comparable in all data, within the possible absolute calibration uncertainty of individual ALMA observations.

## REFERENCES

- Aalto, S., Booth, R. S., Black, J. H., & Johansson, L. E. B. 1995, *A&A*, 300, 369
- Aalto, S., Costagliola, S., Martin F., et al. 2015b, *A&A*, 584, A42
- Aalto, S., Garcia-Burillo, S., Muller, S., et al. 2015a, *A&A*, 574, A85
- Aladro, R., Konig, S., Aalto, S., et al. 2018, *A&A*, 617, A20
- Aladro, R., Martin, S., Riquelme, D., et al. 2015, *A&A*, 579, A101
- Antonucci, R. R. J. 1993, *ARA&A*, 31, 473
- Antonucci, R. R. J. & Miller, J. S. 1985, *ApJ*, 297, 621
- Barbosa, F. K. B., Storchi-Bergmann, T., McGregor, P., Vale, T. B., & Rogemar Riffel, A. 2014, *MNRAS*, 445, 2353
- Barvainis, R. 1987, *ApJ*, 320, 537

- Bauer, F. E., Arevalo, P., Walton, D. J., et al. 2015, *ApJ*, 812, 116
- Bock, J. J., Neugebauer, G., Matthews, K., 2000, *AJ*, 120, 2904
- Cicone, C., Maiolino, R., Sturm, E., et al. 2014, *A&A*, 562, 21
- Costagliola, F., Sakamoto, K., Muller, S., et al. 2015, *A&A*, 582, A91
- Das, V., Crenshaw, D. M., Kraemer, S. B., & Deo, R. P. 2006, *AJ*, 132, 620
- Evans, I. N., Ford, H. C., Kinney, A. L. et al. 1991, *ApJL*, 369, L27
- Ferrarese, L., & Merritt, D. 2000, *ApJL*, 539, L9
- Fukui, Y., & Kawamura, A., 2010, *ARA&A*, 48, 547
- Furuya, R., & Taniguchi, Y., 2016, *PASJ*, 68, 03
- Gallimore, J. F., Baum, S. A., & O’dea, C. P., 2004, *ApJ*, 613, 794
- Gallimore, J. F., Elitzur, M., Maiolino, R., et al. 2016, *ApJL*, 829, L7
- Gao, Y., & Solomon, P. M. 2004, *ApJ*, 606, 271
- Garcia-Burillo, S., Combes, F., Ramos Almeida, C., et al. 2016, *ApJL*, 823, L12
- Garcia-Burillo, S., Combes, F., Ramos Almeida, C., et al. 2019, *A&A*, 632, A61
- Garcia-Burillo, S., Combes, F., Usero, A., et al. 2014, *A&A*, 567, 125
- Garcia-Burillo, S., Combes, F., Usero, A., et al. 2015, *A&A*, 580, A35
- Geballe, T. R., Mason, R. E., Rodriguez-Ardila, A., & Axon, D. J. 2009, *ApJ*, 701, 1710
- Gonzalez-Alfonso, E., Fischer, J., Gracia-Carpio, J., et al. 2014, *A&A*, 561, A27
- Gonzalez-Alfonso, E., & Sakamoto, K. 2019, *ApJ*, 882, 153
- Graninger, D. M., Herbst, E., Öberg, K. I., & Vasyunin, A. I., 2014, *ApJ*, 787, 74
- Gravity Collaboration., Pfuhl, O., Davies, R., et al. 2020, *A&A*, 634, A1
- Greenhill, L. J. & Gwinn, C. R. 1997, *Ap&SS*, 248, 261
- Greenhill, L. J., Gwinn, C. R., Antonucci, R., & Barvainis, R. 1996, *ApJ*, 472, L21
- Harada, N., Thompson, T. A., & Herbst, E. 2013, *ApJ*, 765, 108
- Henkel, C., Asiri, H., Ao, Y., et al. 2014, *A&A*, 565, A3
- Henkel, C., & Mauersberger, R. 1993, *A&A*, 274, 730
- Henkel, C., Mauersberger, R., Wiklind, T., et al. 1993, *A&A*, 268, L17
- Hirota, T., Yamamoto, S., Mikami, H., & Ohishi, M. 1998, *ApJ*, 503, 717
- Honig, S. F. 2019, *ApJ*, 884, 171
- Hure, J. -M. 2002, *A&A*, 395, L21
- Imanishi, M., & Dudley, C. C. 2000, *ApJ*, 545, 701
- Imanishi, M., Dudley, C. C., Maiolino, R., et al. 2007a, *ApJS*, 171, 72
- Imanishi, M., Dudley, C. C., & Maloney, P. R. 2006a, *ApJ*, 637, 114
- Imanishi, M., Nakagawa, T., Ohyama, Y., et al. 2008, *PASJ*, 60, S489
- Imanishi, M., Nakagawa, T., Shirahata, M., Ohyama, Y., & Onaka, T. 2010, *ApJ*, 721, 1233
- Imanishi, M., Nakanishi, K., & Izumi, T. 2016a, *ApJL*, 822, L10
- Imanishi, M., Nakanishi, K., & Izumi, T. 2016b, *ApJ*, 825, 44
- Imanishi, M., Nakanishi, K., & Izumi, T. 2016c, *AJ*, 152, 218
- Imanishi, M., Nakanishi, K., & Izumi, T. 2017, *ApJ*, 849, 29
- Imanishi, M., Nakanishi, K., & Izumi, T. 2018b, *ApJ*, 856, 143
- Imanishi, M., Nakanishi, K., & Izumi, T. 2019, *ApJS*, 241, 19
- Imanishi, M., Nakanishi, K., Izumi, T., & Wada, K. 2018a, *ApJL*, 853, L25
- Imanishi, M., Nakanishi, K., & Kohno, K. 2006b, *AJ*, 131, 2888
- Imanishi, M., Nakanishi, K., Tamura, Y., Oi, N., & Kohno, K. 2007b, *AJ*, 134, 2366
- Imanishi, M., Nakanishi, K., Tamura, Y., & Peng, C. -H. 2009, *AJ*, 137, 3581
- Imanishi, M., Terada, H., Sugiyama, K., et al. 1997, *PASJ*, 49, 69
- Impellizzeri, C. M. V., Gallimore, J. F., Baum, S. A., et al. 2019, *ApJL*, 884, L28
- Izumi, T., Kohno, K., Martin, S., et al. 2013, *PASJ*, 65, 00
- Izumi, T., Kohno, K., Aalto, S., et al. 2016, *ApJ*, 818, 42
- Jiang, X., Wang, J., & Gu, Q. 2011, *MNRAS*, 418, 1753
- Jimenez-Donaire, M. J., Bigiel, F., Leroy, A. K., et al. 2017, *MNRAS*, 466, 49
- Johnson, K. E., Leroy, A. K., Indebetouw, R., et al. 2015, *ApJ*, 806, 35

- Kameno, S., Sawada-Satoh, S., Impellizzeri, C. M. V., et al. 2020, *ApJ*, 895, 73
- Kawakatu, N., Wada, K., & Ichikawa, K. 2020, *ApJ*, 889, 84
- Kohno, K. 2005, in *AIP Conf. Ser.* 783, *The Evolution of Starbursts*, ed. S. Hüttemeister, E. Manthey, D. Bomans, & K. Weis (New York: AIP), 203 (astro-ph/0508420)
- Kormendy, J., & Ho, L. C. 2013, *ARA&A*, 51, 511
- Koyama, K., Inoue, H., Tanaka, Y., et al. 1989, *PASJ*, 41, 731
- Krips, M., Neri, R., Garcia-Burillo, S., Martin, S., Combes, F., Gracia-Carpio, J., & Eckart, A. 2008, *ApJ*, 677, 262
- Krips, M., Martin, S., Eckart, A., et al. 2011, *ApJ*, 736, 37
- Leroy, A. K., Usero, A., Schruba, A., et al. 2017, *ApJ*, 835, 217
- Levenson, N. A., Sirocky, M. M., Hao, L., et al. 2007, *ApJL*, 654, L45
- Lodato, G., & Bertin, G. 2003, *A&A*, 398, 517
- Lopez-Rodriguez, E., Alonso-Herrero, A., Garcia-Burillo, S., et al. 2020, *ApJ*, 893, 33
- Lutz, D., Sturm, E., Janssen, A., et al. 2020, *A&A*, 633, A134
- Maiolino, R., Gallerani, S., Neri, R., et al. 2012, *MNRAS*, 425, L66
- Marinucci, A., Bianchi, S., Matt, G., et al. 2016, *MNRAS*, 456, L94
- Martin, S., Aalto, S., Sakamoto, K., et al. 2016, *A&A*, 590, A25
- Martin, S., Aladro, R., Martin-Pintado, J., & Mauersberger, R. 2010, *A&A*, 522, A62
- Martin, S., Kohno, K., Izumi, T., et al. 2015, *A&A*, 573, A116
- Martin, S., Mauersberger, R., Martin-Pintado, J., et al. 2006, *ApJS*, 164, 450
- Mason, R. E., Geballe, T. R., Packham, C., et al. 2006, *ApJ*, 640, 612
- Matt, G., Guainazzi, M., Frontera, F., et al. 1997, *A&A*, 325, L13
- May, D., & Steiner, J. E. 2017, *MNRAS*, 469, 994
- Meijerink, R., & Spaans, M. 2005, *A&A*, 436, 397
- Meijerink, R., Spaans, M., & Israel, F. P. 2007, *A&A*, 461, 793
- Müller, H. S. P., Schlöder, F., Stutzki, J., Winnewisser, G. 2005, *J. Mol. Struct.*, 742, 215
- Müller Sanchez, F., Davies, R. I., Genzel, R., et al. 2009, *ApJ*, 691, 749
- Nakajima, T., Takano, S., Kohno, K., Harada, N., & Herbst, E. 2018, *PASJ*, 70, 7
- Pereira-Santaella, M., Colina, L., Garcia-Burillo, S., et al. 2018, *A&A*, 616, A171
- Privon, G. C., Herrero-Illana, R., Evans, A. S., et al. 2015, *ApJ*, 814, 39
- Qiu, J., Zhang, J., Zhang, Y., Jia, L., & Tang, X. 2020, *A&A*, 634, A125
- Rangwala, N., Maloney, P. R., Glenn, J., et al. 2011, *ApJ*, 743, 94
- Rhee, J. H., & Larkin, J. E. 2006, *ApJ*, 640, 625
- Roche, P. F., Aitken, D. K., Smith, C. H., & Ward, M. J. 1991, *MNRAS*, 248, 606
- Rybicki, G. B., & Lightman, A. P. 1979, *Radiative Processes in Astrophysics* (New York: Wiley)
- Saito, T., Iono, D., Espada, D., et al. 2018, *ApJ*, 863, 129
- Saito, T., Iono, D., Yun, M. S., et al. 2015, *ApJ*, 803, 60
- Sakamoto, K., Aalto, S., Evans, A. S., Wiedner, M., & Wilner, D. 2010, *ApJ*, 725, L228
- Schilke, P., Walmsley, C. M., Pineau des Forets, G., et al. 1992, *A&A*, 256, 595
- Schinnerer, E., Eckart, A., Tacconi, L. J., Genzel, R., & Downes, D. 2000, *ApJ*, 533, 850
- Shirley, Y. L. 2015, *PASP*, 127, 299
- Solomon, P. M., Rivolo, A. R., Barrett, J., & Yahil, A. 1987, *ApJ*, 319, 730
- Solomon, P. M., & Vanden Bout, P. A. 2005, *ARA&A*, 43, 677
- Spoon, H. W. W., Marshall, J. A., Houck, J. R., et al. 2007, *ApJL*, 654, L49
- Sternberg, A., Genzel, R., & Tacconi, L. 1994, *ApJ*, 436, L131
- Takano, S., Nakajima, T., & Kohno, K. 2019, *PASJ*, 71, S20
- Tanaka, I., Yagi, M., & Taniguchi, Y. 2017, *PASJ*, 69, 90
- Ueno, S., Mushotzky, R. F., Koyama, K., et al. 1994, *PASJ*, 46, L71
- Usero, A., Garcia-Burillo, S., Fuente, A., et al. 2004, *A&A*, 419, 897
- van der Tak, F. F. S., Black, J. H., Schoier, F. L., Jansen, D. J., & van Dishoeck, E. F. 2007, *A&A*, 468, 627
- Viti, S. 2017, *A&A*, 607, A118
- Viti, S., Garcia-Burillo, S., Fuente, A., et al. 2014, *A&A*, 570, A28
- Wada, K. 2012, *ApJ*, 758, 66
- Wada, K., & Norman, C. A. 2007, *ApJ*, 660, 276

Wada, K., Papadopoulos, P. P., & Spaans, M.  
2009, ApJ, 702, 63

Wada, K., Schartmann, M., & Meijerink, R. 2016,  
ApJL, 828, L19

Yamada, M., Wada, K., & Tomisaka, K. 2007,  
ApJ, 671, 73

Zaino, A., Bianchi, S., Marinucci, A., et al. 2020,  
MNRAS, 492, 3872

**Table 1.** Log of ALMA Cycle 6 Observations

Data	Date	Antenna	Baseline	Integration	Calibrator		
	(UT)	Number	(m)	(min)	Bandpass	Flux	Phase
(1)	(2)	(3)	(4)	(5)	(6)	(7)	(8)
data-a	2019 June 6	42	237–15238	47	J0423–0120	J0423–0120	J0239–0234
(HCN/HCO <sup>+</sup> J=3–2)	2019 June 6	42	237–15238	47	J0423–0120	J0423–0120	J0239–0234
	2019 June 6	41	237–15238	47	J0423–0120	J0423–0120	J0239–0234
	2019 June 8	44	83–16196	47	J0423–0120	J0423–0120	J0239–0234
	2019 June 8	44	83–16196	47	J0423–0120	J0423–0120	J0239–0234
	2019 June 8	44	83–16196	47	J0423–0120	J0423–0120	J0239–0234
	2019 June 9	44	83–16196	47	J0006–0623	J0006–0623	J0239–0234
data-b	2019 July 13	46	111–12645	47	J0423–0120	J0423–0120	J0239–0234
( <sup>13</sup> C isotopologue/HNC J=3–2)	2019 July 13	46	111–12645	47	J0423–0120	J0423–0120	J0239–0234
	2019 July 14	43	111–11436	47	J0006–0623	J0006–0623	J0239–0234

NOTE—Col.(1): Data. Data-a include HCN/HCO<sup>+</sup> J=3–2 and their vibrationally excited (HCN-VIB/HCO<sup>+</sup>-VIB) J=3–2 lines. Data-b include HNC/H<sup>13</sup>CN/H<sup>13</sup>CO<sup>+</sup>/HN<sup>13</sup>C/HNC-VIB J=3–2 lines. Col.(2): Observing date in UT. Col.(3): Number of antennas used for observations. Col.(4): Baseline length in meters. Minimum and maximum baseline lengths are shown. Col.(5): Net on source integration time in minutes. Cols.(6), (7), and (8): Bandpass, flux, and phase calibrator for the target source, respectively.

**Table 2.** Continuum Emission

Data	Frequency	Peak flux	Peak coordinate	rms	Synthesized beam
	(GHz)	(mJy/beam)	(RA,DEC)ICRS	(mJy/beam)	(" × ") (°)
(1)	(2)	(3)	(4)	(5)	(6)
data-a	263.6–269.1	6.5 (87 $\sigma$ )	(02 <sup>h</sup> 42 <sup>m</sup> 40.709 <sup>s</sup> , –00° 00′ 47.946″)	0.075	0.019×0.017 (63°)
data-b	256.7–260.5, 270.0–273.7	8.2 (162 $\sigma$ )	(02 <sup>h</sup> 42 <sup>m</sup> 40.709 <sup>s</sup> , –00° 00′ 47.945″)	0.050	0.034×0.026 (53°)

NOTE—Col.(1): Data. Col.(2): Frequency range (in GHz) used to extract continuum emission. Frequencies of obvious emission and absorption lines are excluded. Col.(3): Flux (in mJy beam<sup>–1</sup>) at the emission peak. Value at the highest flux pixel (0′′003 pixel<sup>–1</sup> or 0′′005 pixel<sup>–1</sup>) is adopted. The detection significance relative to the root mean square (rms) noise is shown in parentheses. Possible systematic uncertainties coming from absolute flux calibration ambiguity in individual ALMA observations and choice of frequency range to determine the continuum level are not taken into account. Col.(4): Coordinate of the continuum emission peak in ICRS. Col.(5): The rms noise level (1 $\sigma$ ) (in mJy beam<sup>–1</sup>), derived from the standard deviation of sky signals. Col.(6): Synthesized beam (in arcsec × arcsec) and position angle (in degrees). The position angle is 0° along the north–south direction and increases with the counterclockwise direction.



**Table 3.** Properties of detected molecular lines in the torus region

Position	Line	Integrated intensity (moment 0) map				Gaussian line fit		
		Peak (Jy beam <sup>-1</sup> km s <sup>-1</sup> )	rms (Jy beam <sup>-1</sup> km s <sup>-1</sup> )	Beam (" × ") (°)	Velocity (km s <sup>-1</sup> )	Peak (mJy)	FWHM (km s <sup>-1</sup> )	Flux (Jy km s <sup>-1</sup> )
(1)	(2)	(3)	(4)	(5)	(6)	(7)	(8)	(9)
E-peak	HCN J=3-2	0.26 (7.3σ)	0.036	0.021 × 0.018 (59)	1099±7	1.1±0.1	193±18	0.23±0.03
	HCO <sup>+</sup> J=3-2	0.29 (10σ)	0.028	0.021 × 0.018 (60)	1094±9	0.90±0.08	225±34	0.22±0.04
W-peak	HCN J=3-2	0.45 (13σ)	0.036	0.021 × 0.018 (59)	1160±12	1.0±0.1	408±30	0.45±0.04
					1088±10, 1192±19	0.53±0.12, 0.83±0.08	104±33, 456±37	0.46±0.06
	HCO <sup>+</sup> J=3-2	0.33 (11σ)	0.028	0.021 × 0.018 (60)	1179±15	0.72±0.05	393±42	0.30±0.04
					1109, 1223 (fix) <sup>A</sup>	0.49±0.15, 0.52±0.07	86, 498 (fix) <sup>A</sup>	0.32±0.04
	HCN-VIB J=3-2	0.049(4.8σ) <sup>B</sup>	0.010	0.021 × 0.018 (60)	1339±7	0.35±0.05	109±20	0.041±0.009
Close to C-peak <sup>C</sup>	H <sup>13</sup> CN J=3-2	-0.090 (4.5σ) <sup>C</sup>	0.020	0.035 × 0.029 (60)				
Close to W-peak <sup>D</sup>	HNC J=3-2	0.091 (3.6σ) <sup>D</sup>	0.025	0.036 × 0.026 (54)				

<sup>A</sup>Fixed to the best fit value.

<sup>B</sup>The highest positive value in the western torus (Figure 15) is found at (02<sup>h</sup> 42<sup>m</sup> 40.708<sup>s</sup>, -00° 00' 47.937'').

<sup>C</sup>The most negative signal close to the C-peak (Figure 9a) is found at (02<sup>h</sup> 42<sup>m</sup> 40.710<sup>s</sup>, -00° 00' 47.945''). This spatially agrees with the C-peak within the position determination accuracy of (beam-size)/(signal-to-noise-ratio) ~ 0'007.

<sup>D</sup>The highest positive value in the western torus (Figure 9b) is found at (02<sup>h</sup> 42<sup>m</sup> 40.708<sup>s</sup>, -00° 00' 47.945'').

NOTE—Col.(1): Position. C-peak (continuum emission peak): (02<sup>h</sup> 42<sup>m</sup> 40.709<sup>s</sup>, -00° 00' 47.946''), E-peak (HCN J=3-2 emission peak in the eastern torus): (02<sup>h</sup> 42<sup>m</sup> 40.710<sup>s</sup>, -00° 00' 47.952''). W-peak (HCN J=3-2 emission peak in the western torus): (02<sup>h</sup> 42<sup>m</sup> 40.708<sup>s</sup>, -00° 00' 47.940''). Col.(2): Molecular line. Col.(3): Integrated intensity (in Jy beam<sup>-1</sup> km s<sup>-1</sup>) at the emission peak. The detection significance relative to the rms noise (1σ) in the moment 0 map is shown in parentheses. Possible systematic uncertainty is not included. Col.(4): The rms noise (1σ) level in the moment 0 map (in Jy beam<sup>-1</sup> km s<sup>-1</sup>), derived from signals in the annular region with 2'4-6'0 in radius centered at (02<sup>h</sup>42<sup>m</sup>40.70<sup>s</sup>, -00°00'48.5'') to avoid areas of significant molecular line emission. Col.(5): Beam size (in arcsec × arcsec) and position angle (in degrees). Position angle is 0° along the north-south direction, and increases counterclockwise. Cols.(6)–(9): Gaussian fit of clearly detected emission lines in beam-sized spectra. At the W-peak, two Gaussian fits are applied because a very broad component is observed, in addition to a narrow component. Col.(6): Optical LSR velocity of emission peak (in km s<sup>-1</sup>). Col.(7): Peak flux (in mJy). Col.(8): Observed FWHM (in km s<sup>-1</sup>) in the spectra of Fig. 5. Col.(9): Gaussian-fit, velocity-integrated flux (in Jy km s<sup>-1</sup>). At the W-peak, the single and two Gaussian fits provide comparable flux values both for HCN J=3-2 and HCO<sup>+</sup> J=3-2 lines. We adopt the single Gaussian fit results for our discussion.

**Table 4.** Properties of HCN J=3–2 and HCO<sup>+</sup> J=3–2 emission lines in area-integrated torus spectra

Region	Line	Gaussian line fit			
		Velocity (km s <sup>-1</sup> )	Peak (mJy)	FWHM (km s <sup>-1</sup> )	Flux (Jy km s <sup>-1</sup> )
(1)	(2)	(3)	(4)	(5)	(6)
Torus (0''2 × 0''1)	HCN J=3–2	1135±2	17±1	190±7	3.4±0.1
	HCO <sup>+</sup> J=3–2	1129±4	11±1	189±9	2.2±0.1
E-torus (0''1 × 0''1)	HCN J=3–2	1137±2	10±1	171±6	1.9±0.1
	HCO <sup>+</sup> J=3–2	1133±4	6.8±0.3	170±10	1.2±0.1
W-Torus (0''1 × 0''1)	HCN J=3–2	1137±5	6.6±0.3	236±14	1.6±0.1
	HCO <sup>+</sup> J=3–2	1122±7	4.6±0.3	213±24	1.0±0.1

NOTE—Col.(1): Region. Col.(2): Line. Cols.(3)–(6): Gaussian fit of emission lines in area-integrated torus spectra. Col.(3): Optical LSR velocity of emission peak (in km s<sup>-1</sup>). Col.(4): Peak flux (in mJy). Col.(5): Observed FWHM (in km s<sup>-1</sup>). Col.(6): Gaussian-fit, velocity-integrated flux (in Jy km s<sup>-1</sup>).

**Table 5.** HCN J=3–2 and HCO<sup>+</sup> J=3–2 emission line luminosity and estimated dense molecular mass in the 14 pc × 7 pc torus region

Line	L	L'	M <sub>dense</sub>
(1)	10 <sup>2</sup> (L <sub>⊙</sub> )	10 <sup>5</sup> (K km s <sup>-1</sup> pc <sup>2</sup> )	10 <sup>6</sup> (M <sub>⊙</sub> )
(1)	(2)	(3)	(4)
HCN J=3–2	1.8	3.1	2–4
HCO <sup>+</sup> J=3–2	1.2	2.0	0.4–1.0

NOTE— Col.(1): Line. Col.(2): Luminosity (in L<sub>⊙</sub>). Col.(3): Luminosity (in K km s<sup>-1</sup> pc<sup>2</sup>). Col.(4): Estimated dense molecular mass (in M<sub>⊙</sub>).

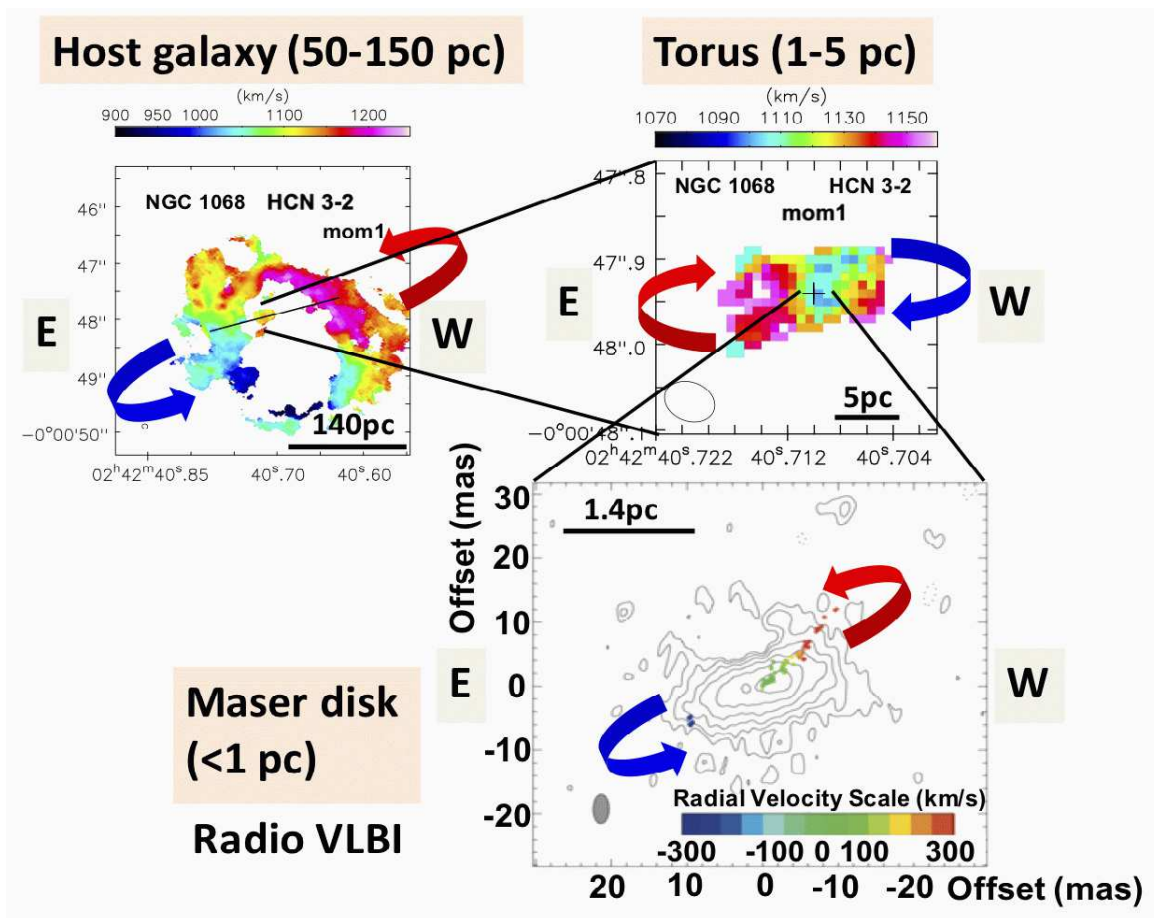


**Figure 1.** Observed dynamical properties of dense molecular and H<sub>2</sub>O maser emission at the inner part of NGC 1068. (*Top Left*): Intensity-weighted rotation velocity (moment 1) map of HCN J=3-2 emission line in the host galaxy (50–150 pc) scale (Imanishi et al. 2018a). The thin solid line crossing the torus at the center indicates the torus axis (PA  $\sim 105^\circ$ ). (*Top Right*): Moment 1 map of HCN J=3-2 in the torus (1–5 pc) scale (Imanishi et al. 2018a). (*Bottom*): H<sub>2</sub>O maser emission dynamics at the innermost ( $\lesssim 1$  pc) part. Modified from Gallimore et al. (2004). Velocity relative to their adopted systemic velocity is color coded. The coordinates are offset (in mas) from the VLBA 5 GHz continuum shown as contours. North is up and east is to the left in all plots. The length of the thick horizontal bar corresponds to 140 pc, 5 pc, 1.4 pc in the top-left, top-right, bottom panel, respectively. Thick curved blue and red arrows indicate blueshifted and redshifted motion relative to the systemic velocity of NGC 1068, respectively. The western side is *redshifted* for maser emission at  $\lesssim 1$  pc (*bottom*) and dense molecular emission in the host galaxy at 50–150 pc scale (*top left*), but is *blueshifted* for the torus dense molecular emission at 1–5 pc scale (*top right*).

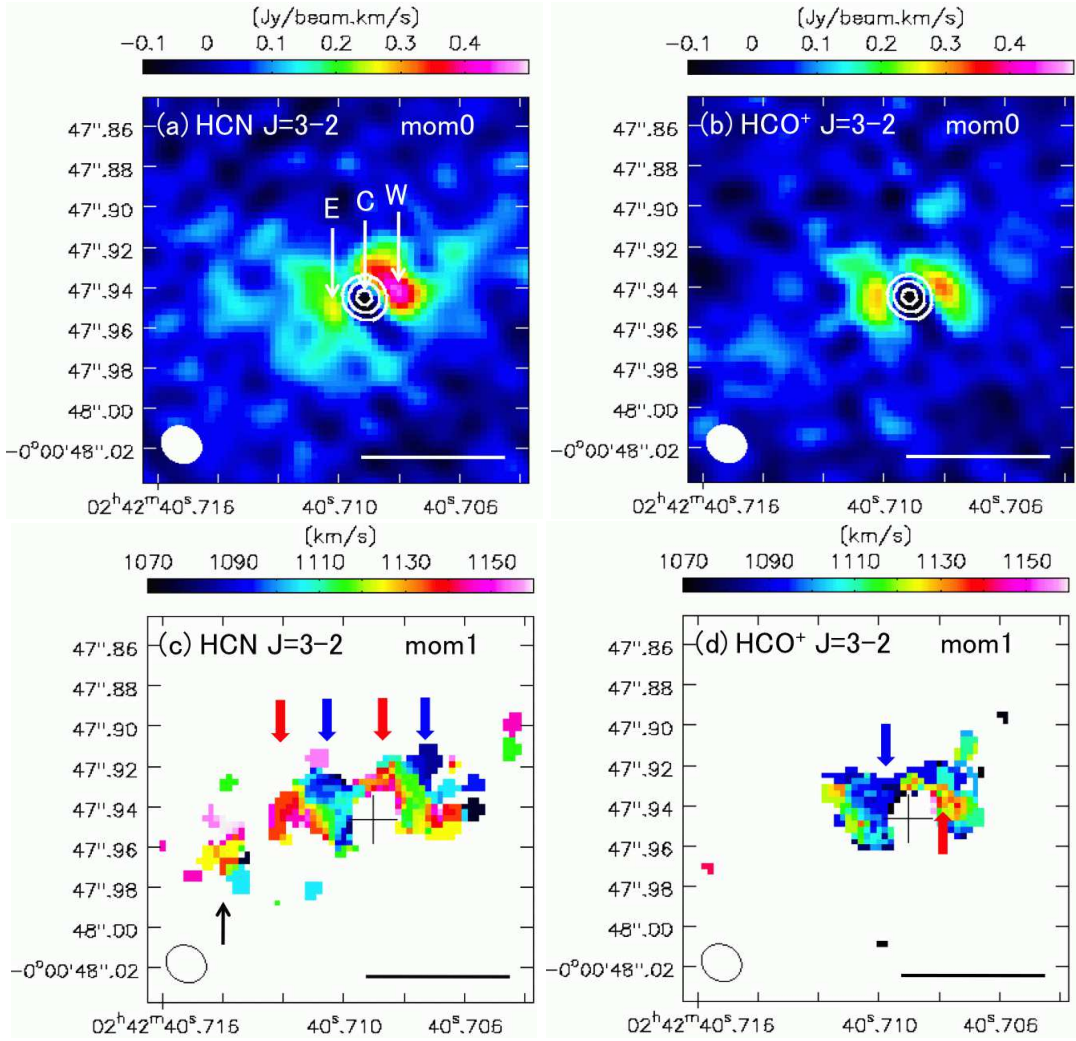


**Figure 2.** (*Top*): Integrated intensity (moment 0) maps of (a) HCN J=3–2 and (b) HCO<sup>+</sup> J=3–2 lines, overlaid on the contours of  $\sim 260$  GHz ( $\sim 1.2$  mm) continuum emission ( $40$ ,  $60$ , and  $80\sigma$ ;  $1\sigma = 0.075$  mJy beam<sup>-1</sup>). The color scale is the same between these two lines ( $-0.1$  to  $+0.5$  Jy beam<sup>-1</sup> km s<sup>-1</sup>). In (a), E-, C-, and W-peaks (Table 3) are indicated with thin white downward arrows, with the notes of “E”, “C”, and “W”, respectively. The horizontal white bar at the lower right part of each figure indicates 5 pc at the distance of NGC 1068. Beam size is shown as a filled circle in the lower-left region. (*Bottom*): Intensity-weighted mean velocity (moment 1) maps of (c) HCN J=3–2 and (d) HCO<sup>+</sup> J=3–2 emission lines. The black cross denotes the location of the continuum emission peak ( $02^{\text{h}} 42^{\text{m}} 40.709^{\text{s}}$ ,  $-00^{\circ} 00' 47.946''$ ), which is taken as the mass-accreting SMBH location. The velocity display range (optical LSR velocity  $V_{\text{opt}}[\text{LSR}] = 1070\text{--}1160$  km s<sup>-1</sup> or from  $V_{\text{sys}} - 60$  to  $V_{\text{sys}} + 30$  km s<sup>-1</sup>, where  $V_{\text{sys}}$  is the systemic velocity of  $1130$  km s<sup>-1</sup>) is set in the same way as adopted by Imanishi et al. (2018a), to see blueshifted and redshifted velocity components significantly slower than the Keplerian rotation at 2–5 pc from the mass-dominating SMBH ( $M_{\text{SMBH}} \sim 1 \times 10^7 M_{\odot}$ ). For the HCN J=3–2 emission, inner redshifted and outer blueshifted emission components in the western torus are marked with thick red and blue downward arrows, respectively. Inner blueshifted and outer redshifted emission components in the eastern torus are also indicated as thick blue and red downward arrows, respectively. Eastern emission at RA =  $02^{\text{h}} 42^{\text{m}} 40.714^{\text{s}}$  (discussed in §4.6) is indicated as a black upward arrow. For the HCO<sup>+</sup> J=3–2 emission, inner redshifted and blueshifted emission in the western and eastern torus, respectively, are indicated as thick red upward and blue downward arrows. The horizontal black bar at the lower right part of each figure indicates 5 pc at the distance of NGC 1068. Beam size is shown as an open circle in the lower-left region. An appropriate cutoff ( $\sim 4\sigma$ ) is applied to moment 1 maps in (c) and (d) so that they are not dominated by noise.

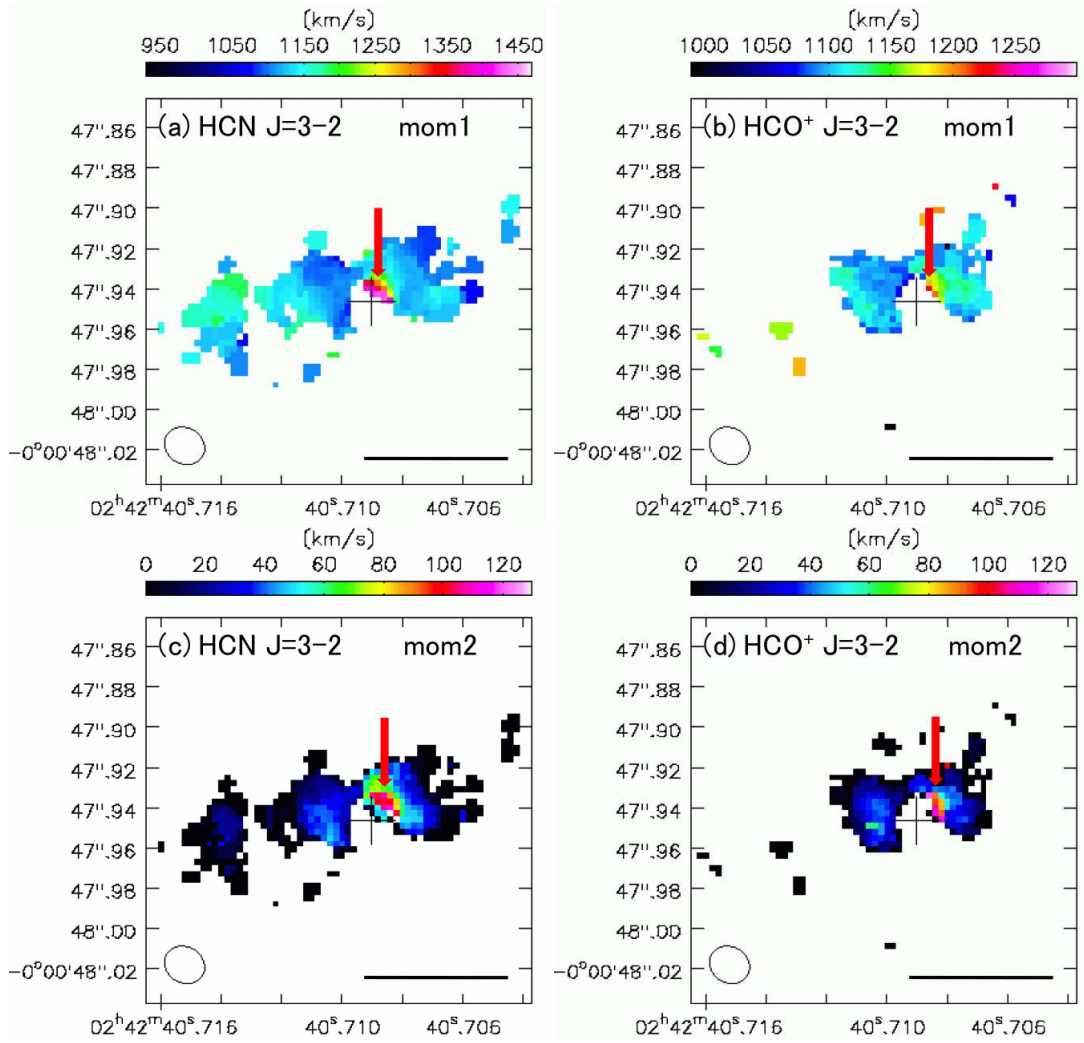


**Figure 3.** (*Top*): Intensity-weighted mean velocity (moment 1) maps of (a) HCN J=3–2 and (b) HCO<sup>+</sup> J=3–2 emission lines. The velocity display range is 930–1470 km s<sup>−1</sup> (from  $V_{\text{sys}} - 200$  to  $V_{\text{sys}} + 340$  km s<sup>−1</sup>) for (a) HCN J=3–2, to display a redshifted high velocity ( $\gtrsim 1300$  km s<sup>−1</sup> or  $V_{\text{sys}} + [\gtrsim 170]$  km s<sup>−1</sup>) emission component at the innermost western torus. The range is 990–1300 km s<sup>−1</sup> (from  $V_{\text{sys}} - 140$  to  $V_{\text{sys}} + 170$  km s<sup>−1</sup>) for (b) HCO<sup>+</sup> J=3–2. The black cross and horizontal black bar indicate the location of the continuum emission peak (= SMBH position) and 5 pc at the distance of NGC 1068, respectively. The innermost redshifted component in the western torus is indicated as a thick red downward arrow. Beam size is shown as an open circle in the lower-left region. (*Bottom*): Intensity-weighted velocity dispersion (moment 2) maps of (c) HCN J=3–2 and (d) HCO<sup>+</sup> J=3–2 emission lines. The velocity display range is 0–130 km s<sup>−1</sup> for both lines. The black cross, horizontal black bar, and open circle have the same meanings as in the top panels. The high velocity dispersion region in the western torus is indicated as a thick red downward arrow. For all maps in (a–d), an appropriate cutoff ( $\sim 4\sigma$ ) is applied to prevent them from being overwhelmed by noise.

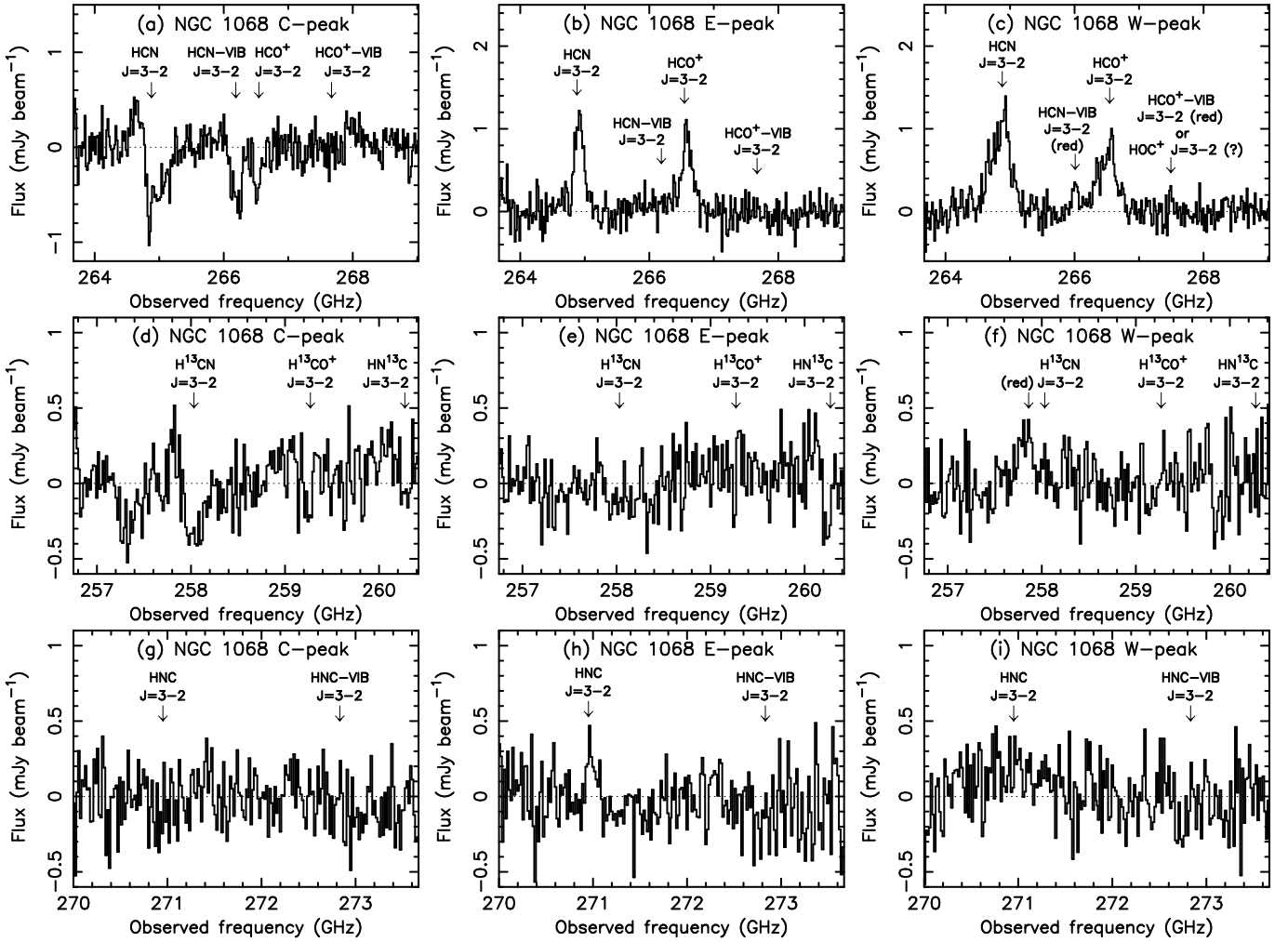


**Figure 4.** (a), (b), (c): Spectra of data-a (HCN/HCO<sup>+</sup> J=3–2 observations), within the beam size ( $\sim 0''.02$ ), at the C-peak, E-peak, and W-peak, respectively. Some targeted lines are indicated with downward arrows at  $V_{\text{sys}} = 1130 \text{ km s}^{-1}$ . In the spectrum at (c) W-peak, downward arrows are added at  $V = 1340 \text{ km s}^{-1}$  ( $V_{\text{sys}} + 210 \text{ km s}^{-1}$ ) for HCN-VIB J=3–2 and HCO<sup>+</sup>-VIB J=3–2 lines with the note of “(red)”, to represent redshifted emission component at the innermost western torus (see §4.3 and 4.5). (d), (e), (f): Lower frequency part of the spectrum of data-b (<sup>13</sup>C isotopologue/HNC J=3–2 observations), within the beam size ( $\sim 0''.03$ ), at the C-peak, E-peak, and W-peak, respectively. In (f), a downward arrow is added at  $V = 1340 \text{ km s}^{-1}$  ( $V_{\text{sys}} + 210 \text{ km s}^{-1}$ ) for H<sup>13</sup>CN J=3–2 with the note of “(red)”. (g), (h), (i): Higher frequency part of the beam-sized ( $\sim 0''.03$ ) spectrum of data-b at the C-peak, E-peak, and W-peak, respectively. Note that the beam size is slightly larger for data-b (see Tables 2 and 3). In all plots, the abscissa is observed frequency (in GHz) and the ordinate is flux density (in mJy beam<sup>-1</sup>). The thin dotted horizontal straight line indicates the zero flux level.



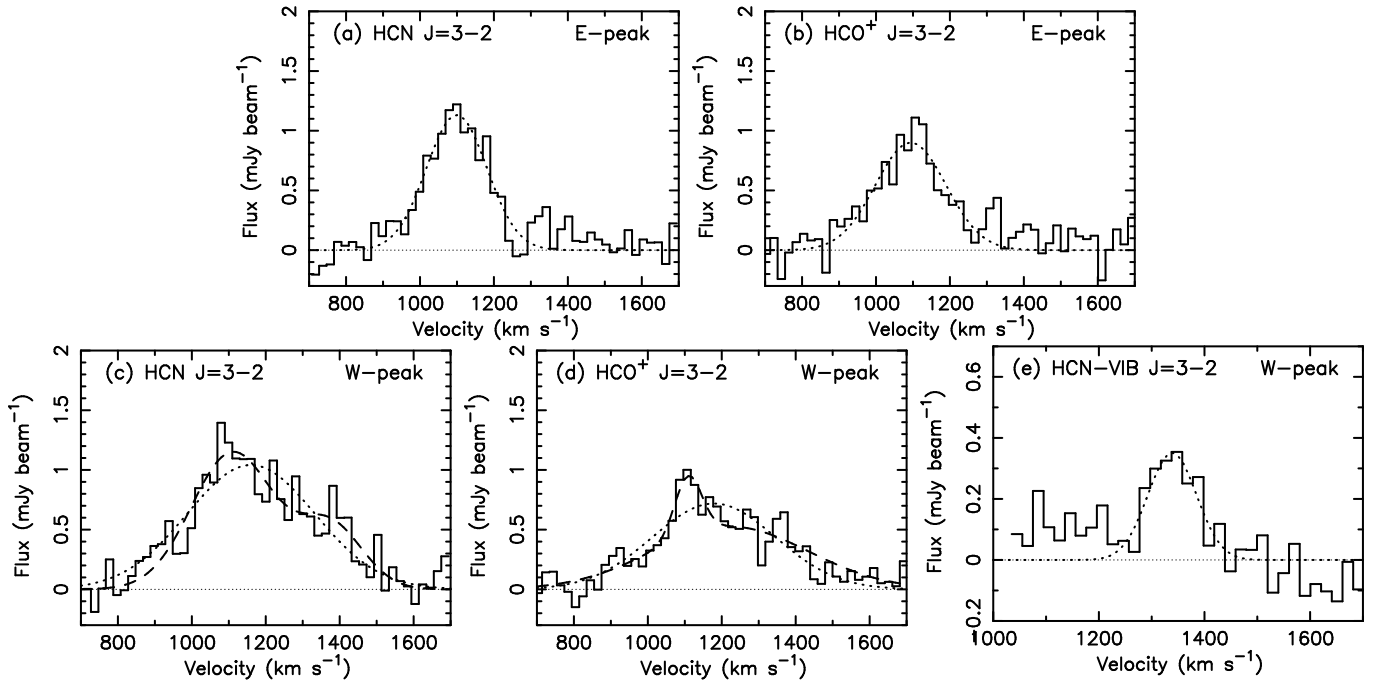


**Figure 5.** Gaussian fit of detected molecular emission line in the beam-sized spectrum. (a): HCN J=3–2 at the eastern torus peak (E-peak). (b): HCO<sup>+</sup> J=3–2 at the E-peak. (c): HCN J=3–2 at the western torus peak (W-peak). (d): HCO<sup>+</sup> J=3–2 at the W-peak. (e): HCN-VIB J=3–2 at the W-peak. The abscissa is optical LSR velocity (in km s<sup>-1</sup>) and the ordinate is flux density (in mJy beam<sup>-1</sup>). Single Gaussian fit is shown as curved dotted line. For the HCN J=3–2 and HCO<sup>+</sup> J=3–2 emission lines at the W-peak, two Gaussian fit is also added with curved dashed line. The thin dotted horizontal straight line indicates the zero flux level.

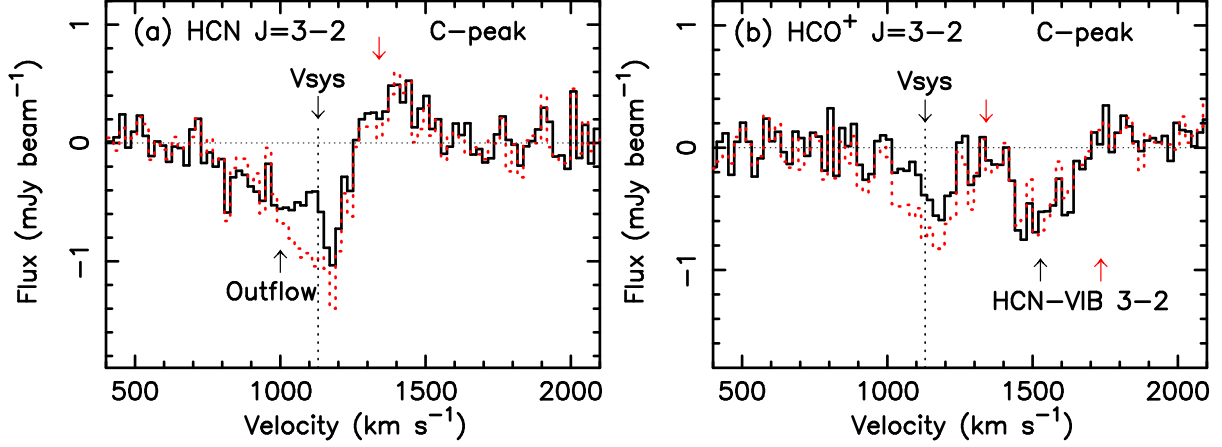


**Figure 6.** Velocity profile of (a) HCN  $J=3-2$  and (b)  $\text{HCO}^+$   $J=3-2$  lines at the C-peak. The black solid line indicates an observed spectrum within the beam size. The red dotted line is a spectrum after an attempt to correct for the possible emission contamination from the innermost parts of the western and eastern torus (see §4.7). The abscissa is optical LSR velocity (in  $\text{km s}^{-1}$ ) and the ordinate is flux density (in  $\text{mJy beam}^{-1}$ ). The thin dotted horizontal straight line indicates the zero flux level. The systemic velocity ( $1130 \text{ km s}^{-1}$ ) is shown as a vertical dotted line with the note of “ $V_{\text{sys}}$ ”. A red downward arrow is added at the velocity of  $V = 1340 \text{ km s}^{-1}$  ( $V_{\text{sys}} + 210 \text{ km s}^{-1}$ ) to indicate redshifted emission at the innermost western torus (see §4.5). In (a), a blueshifted broad absorption feature (discussed in §4.7) is indicated with a black upward arrow with the note of “Outflow”. In (b), a black and red upward arrow with the note of “HCN-VIB 3-2” indicates HCN-VIB  $J=3-2$  line at  $V_{\text{sys}} = 1130 \text{ km s}^{-1}$  and  $V = 1340 \text{ km s}^{-1}$  ( $V_{\text{sys}} + 210 \text{ km s}^{-1}$ ), respectively.

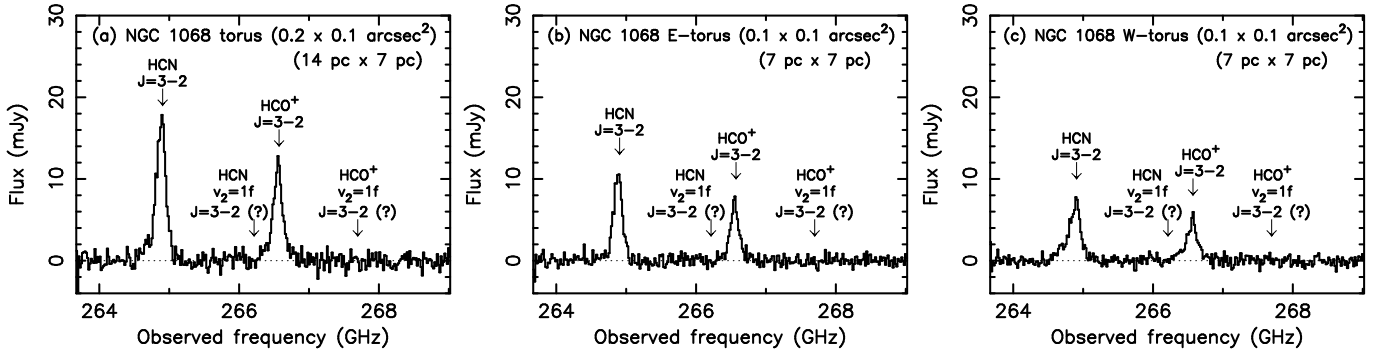


**Figure 7.** (a): An area-integrated spectrum of HCN  $J=3-2$  and  $\text{HCO}^+$   $J=3-2$  emission lines with  $0''.2$  east-west and  $0''.1$  north-south ( $14 \text{ pc} \times 7 \text{ pc}$ ) rectangular region centered at the C-peak. (b): An area-integrated spectrum of  $0''.1 \times 0''.1$  square region in the eastern torus (E-torus; eastern half of the rectangular region). (c): An area-integrated spectrum of  $0''.1 \times 0''.1$  square region in the western torus (W-torus; western half of the rectangular region). The abscissa is observed frequency (in GHz) and the ordinate is flux density (in mJy). The thin dotted horizontal straight line indicates the zero flux level.

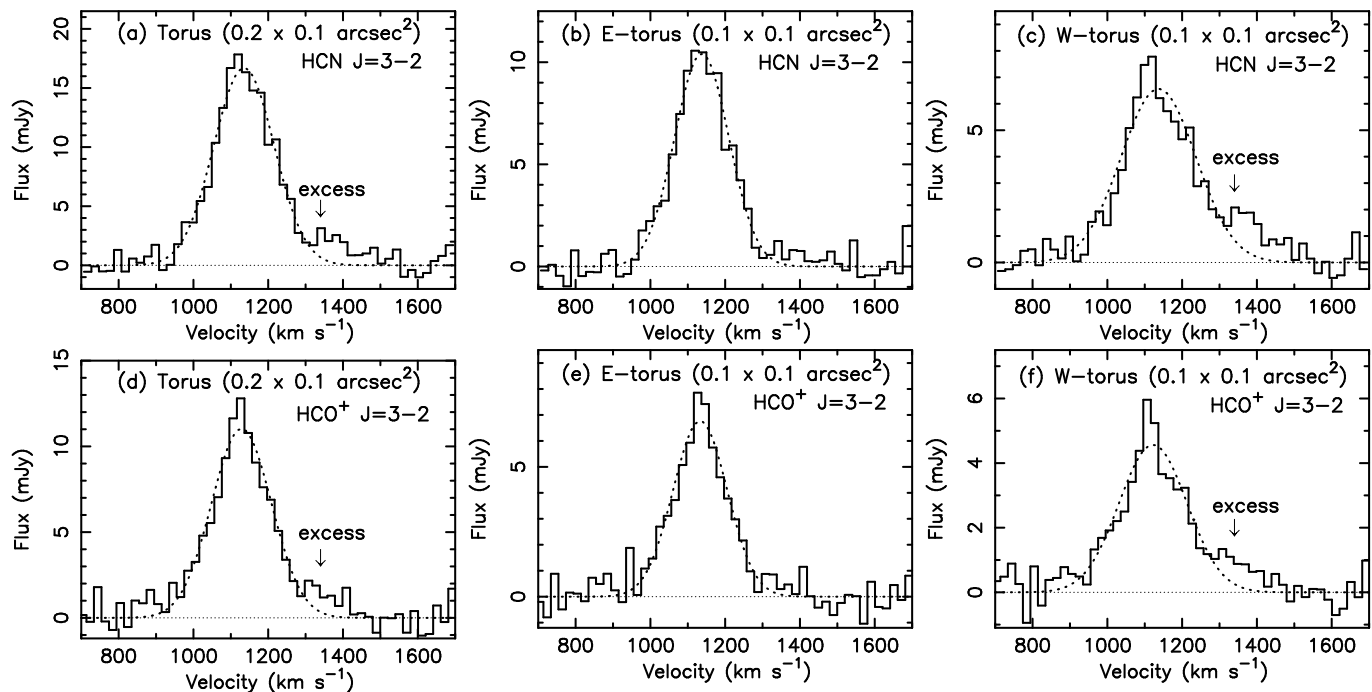


**Figure 8.** Gaussian fits of (*Top*) HCN J=3–2 and (*Bottom*) HCO<sup>+</sup> J=3–2 emission lines in area-integrated spectra shown in Figure 7. (a), (b), (c): HCN J=3–2 emission from the torus (0<sup>0</sup>.2 × 0<sup>0</sup>.1 [= 14 pc × 7 pc] rectangular region), E-torus (0<sup>0</sup>.1 × 0<sup>0</sup>.1 square region), and W-torus (0<sup>0</sup>.1 × 0<sup>0</sup>.1 square region), respectively. (d), (e), (f): HCO<sup>+</sup> J=3–2 emission from the torus, E-torus, and W-torus, respectively. The abscissa is optical LSR velocity (in km s<sup>-1</sup>) and the ordinate is flux density (in mJy). The thin dotted horizontal straight line indicates the zero flux level. Single Gaussian fit is shown with a curved dotted line. Redshifted excess emission, relative to the Gaussian component (discussed in §4.3), is indicated with a downward arrow with the note of “excess”.

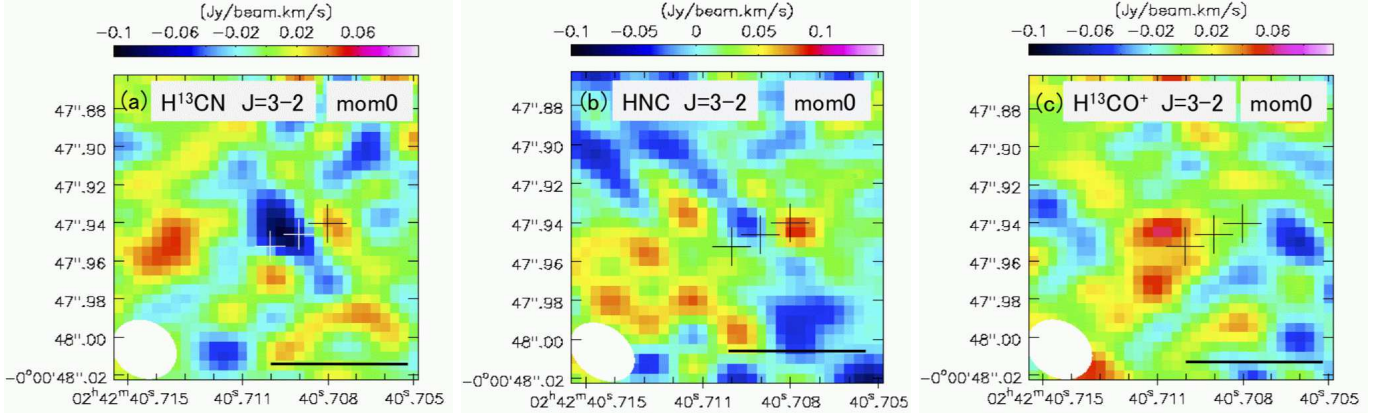


**Figure 9.** Integrated intensity (moment 0) map of (a)  $\text{H}^{13}\text{CN}$   $J=3-2$ , (b)  $\text{HNC}$   $J=3-2$ , and (c)  $\text{H}^{13}\text{CO}^+$   $J=3-2$ . Three cross marks are added at the E-peak, C-peak, and W-peak (Table 3) from the left to the right. In all maps, signals in the same velocity range ( $920\text{--}1320\text{ km s}^{-1}$  or from  $V_{\text{sys}} - 210$  to  $V_{\text{sys}} + 190\text{ km s}^{-1}$ ) are integrated. The rms noise level is 0.020, 0.025, and 0.024 ( $\text{Jy beam}^{-1}\text{ km s}^{-1}$ ) for (a)  $\text{H}^{13}\text{CN}$   $J=3-2$ , (b)  $\text{HNC}$   $J=3-2$ , and (c)  $\text{H}^{13}\text{CO}^+$   $J=3-2$ , respectively. For (a)  $\text{H}^{13}\text{CN}$   $J=3-2$ , a clear negative (i.e., absorption) signal ( $4.5\sigma$ ; blue colored) is recognizable close to the C-peak (middle cross). For (b)  $\text{HNC}$   $J=3-2$ , an emission signal (red colored) is seen close to the W-peak (right cross) with  $3.6\sigma$ . For (a) and (b), any other possible emission/absorption signatures are insignificant ( $<3\sigma$ ). For (c)  $\text{H}^{13}\text{CO}^+$   $J=3-2$ , neither emission nor absorption signal is significant in the torus region ( $<3\sigma$ ). The horizontal black bar at the lower-right side indicates 5 pc at the distance of NGC 1068. Beam size is shown as a filled circle in the lower-left region.

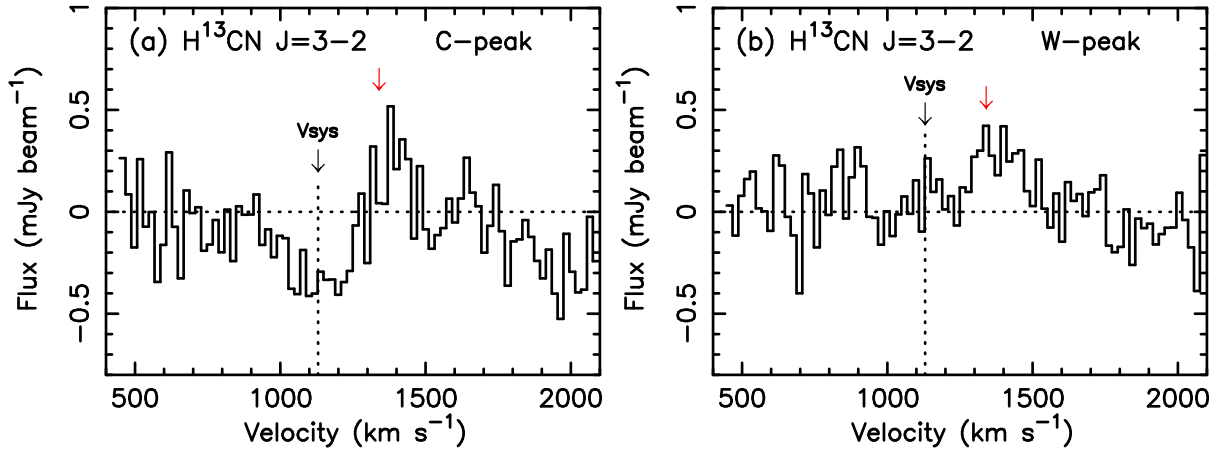


**Figure 10.** Velocity profile of  $\text{H}^{13}\text{CN}$   $J=3-2$  line at the (a) C-peak and (b) W-peak. The abscissa is optical LSR velocity (in  $\text{km s}^{-1}$ ) and the ordinate is flux density (in  $\text{mJy beam}^{-1}$ ). The thin dotted horizontal straight line indicates the zero flux level. The systemic velocity ( $1130\text{ km s}^{-1}$ ) is shown as a vertical dotted line with the note of “ $V_{\text{sys}}$ ”. A red downward arrow is added at  $V = 1340\text{ km s}^{-1}$  ( $V_{\text{sys}} + 210\text{ km s}^{-1}$ ), as in Figure 6.

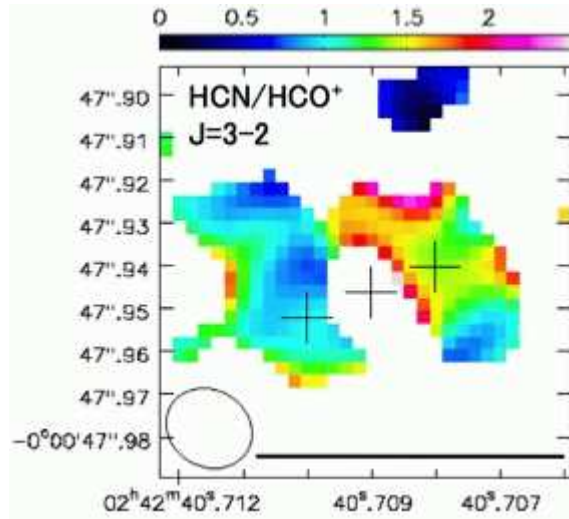


**Figure 11.** The ratio of HCN J=3-2 flux to HCO<sup>+</sup> J=3-2 flux (in Jy beam<sup>-1</sup> km s<sup>-1</sup>). Only pixels with  $>3\sigma$  HCO<sup>+</sup> J=3-2 detection (i.e., denominator) in the moment 0 map in Figure 2b are shown. Thus, this ratio map does not preferentially pick up elevated HCN emission regions only. Three cross marks are added at the E-peak, C-peak, and W-peak (Table 3) from the left to the right. The horizontal black bar at the lower-right side indicates 5 pc at the distance of NGC 1068. Beam size is shown as an open circle in the lower-left region.

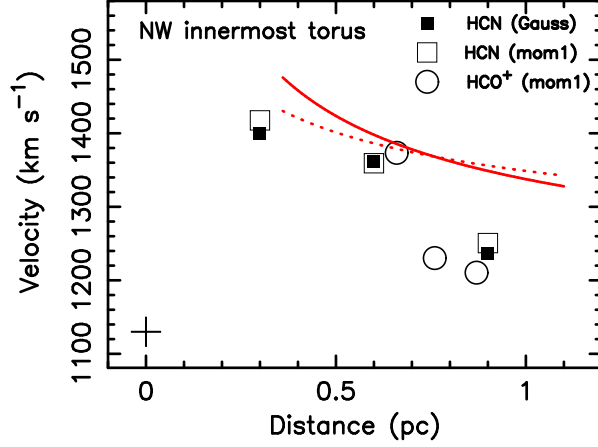


**Figure 12.** Velocity of the redshifted HCN J=3–2 and HCO<sup>+</sup> J=3–2 emission lines at the innermost northwestern torus. The abscissa is projected distance from the central SMBH (in pc), and the ordinate is velocity (in km s<sup>−1</sup>). The plus mark indicates the systemic velocity ( $V_{\text{sys}} = 1130$  km s<sup>−1</sup>) at the SMBH position. Filled square: HCN J=3–2 velocity based on the Gaussian fit of beam-sized spectrum extracted at each distance from the central SMBH. Open square: HCN J=3–2 intensity-weighted velocity derived from moment 1 map (Figure 3a). Open circle: HCO<sup>+</sup> J=3–2 intensity-weighted velocity from moment 1 map (Figure 3b). HCN J=3–2 line velocity is measured along PA = 135° east of north. HCO<sup>+</sup> J=3–2 line velocity is measured along PA = 105–120°, because strong HCO<sup>+</sup> J=3–2 emission is detected along this direction. The Gaussian fit of the HCO<sup>+</sup> J=3–2 emission line is not shown, owing to large uncertainty caused by a strong absorption feature at 1400–1700 km s<sup>−1</sup> (or  $V_{\text{sys}} + [270\text{--}570]$  km s<sup>−1</sup>) seen in Figure 6b. The red solid and dotted lines mean, respectively, Keplerian motion ( $V \propto r^{-0.5}$ ) with the central SMBH mass of  $\sim 1 \times 10^7 M_{\odot}$  (Greenhill et al. 1996) and inclination  $i = 90^{\circ}$  (edge-on), and sub-Keplerian motion with  $V \propto r^{-0.31}$  ( $i = 90^{\circ}$ ) that reproduces  $\sim 250$  km s<sup>−1</sup> rotation velocity at  $\sim 0.65$  pc (Greenhill et al. 1996).

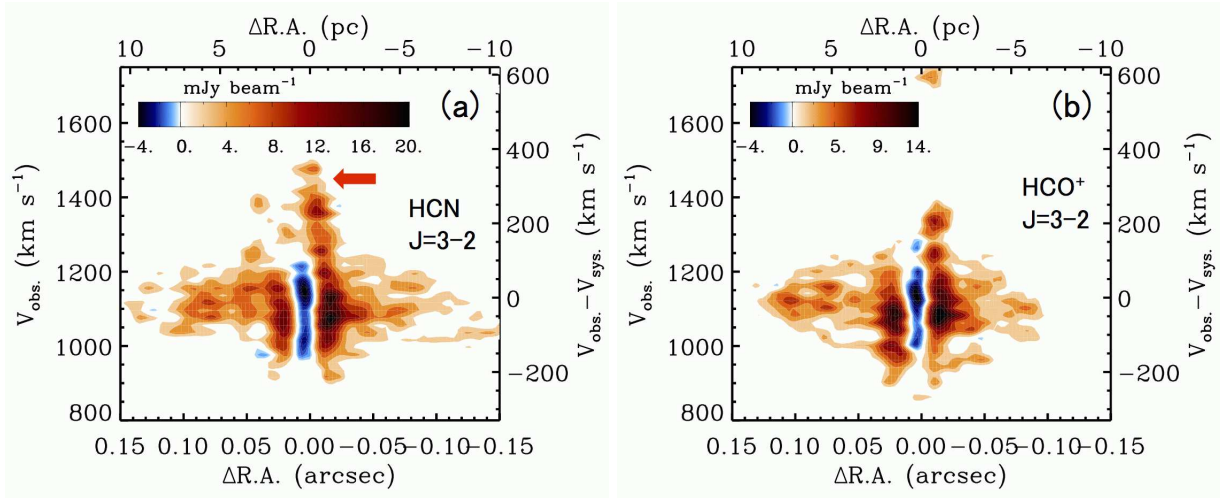


**Figure 13.** Position velocity diagram of (a) HCN J=3-2 and (b) HCO<sup>+</sup> J=3-2 lines along PA = 115° east of north. The abscissa is offset from the SMBH position in arcsec (bottom) and in pc (top). The ordinate is optical LSR velocity (in km s<sup>-1</sup>; left) and velocity relative to the systemic one of  $V_{\text{sys}} = 1130$  km s<sup>-1</sup> (in km s<sup>-1</sup>; right). Southeast is to the left and northwest is to the right. The thick red leftward arrow in (a) indicates the redshifted high velocity ( $V \sim 1300\text{--}1500$  km s<sup>-1</sup> or  $V_{\text{sys}} + [170\text{--}370]$  km s<sup>-1</sup>) HCN J=3-2 emission component at the innermost northwestern torus discussed in §4.3. In (b), signal at the very top ( $V \gtrsim 1700$  km s<sup>-1</sup> or  $V_{\text{sys}} + [\gtrsim 570]$  km s<sup>-1</sup>) is not from the HCO<sup>+</sup> J=3-2 line, but from the redshifted HCN-VIB J=3-2 line emitted at the innermost northwestern torus (Figure 6b).

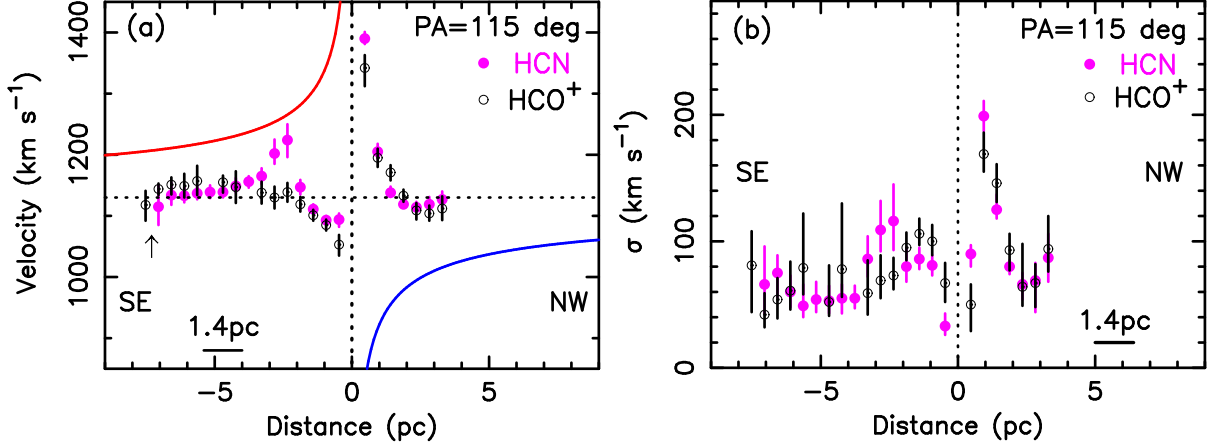


**Figure 14.** (a): Velocity of inner to outer torus, along PA  $\sim 115^\circ$ , based on Gaussian fit of beam-sized spectrum extracted at each position. The abscissa is projected distance from the central SMBH (in pc) and the ordinate is peak velocity,  $V_c$  (in  $\text{km s}^{-1}$ ), of the Gaussian function of  $A \times \exp(-[V - V_c]^2 / 2\sigma^2)$ , where  $A$  is a constant,  $V$  is velocity (in  $\text{km s}^{-1}$ ), and  $\sigma$  is emission line width (in  $\text{km s}^{-1}$ ). The thin dotted vertical and horizontal straight line indicates SMBH position and systemic velocity ( $V_{\text{sys}} = 1130 \text{ km s}^{-1}$ ), respectively. Magenta filled circle: HCN J=3–2. Black open circle:  $\text{HCO}^+$  J=3–2. Southeast is to the left and northwest is to the right. Peak velocity uncertainty based on the Gaussian fit is  $\lesssim 20 \text{ km s}^{-1}$  in almost all points, except for a few points with faint molecular line emission where the uncertainty is  $\sim 30 \text{ km s}^{-1}$ . Data points with uncertainty  $\gtrsim 30 \text{ km s}^{-1}$  are excluded. The red and blue solid curved lines are Keplerian velocity for the central SMBH mass of  $1 \times 10^7 M_\odot$  ( $i = 90^\circ$ ), with the eastern (western) part being redshifted (blueshifted). The thin black upward arrow indicates abrupt velocity change from redshifted to blueshifted motion at  $\sim 7$  pc southeastern side of the SMBH (discussed in §4.6). The redshifted components at 0–1 pc (just right side of the SMBH) correspond to the redshifted dense molecular line emission at the innermost northwestern torus (§4.3). The velocity of the redshifted innermost northwestern  $\text{HCO}^+$  J=3–2 data point (black open circle just right side of the SMBH) can be largely affected by the HCN-VIB J=3–2 absorption feature (Figure 6b). Blueshifted components are also seen at the innermost ( $\lesssim 1$  pc) southeastern torus (just left side of the SMBH), although its velocity, relative to the systemic, is smaller than that in the northwestern side. The horizontal solid bar at the lower part is our beam size ( $\sim 0''.02$  or  $\sim 1.4$  pc). (b): Same as (a), but the ordinate is emission line velocity width,  $\sigma$  (in  $\text{km s}^{-1}$ ), of  $A \times \exp(-[V - V_c]^2 / 2\sigma^2)$ .



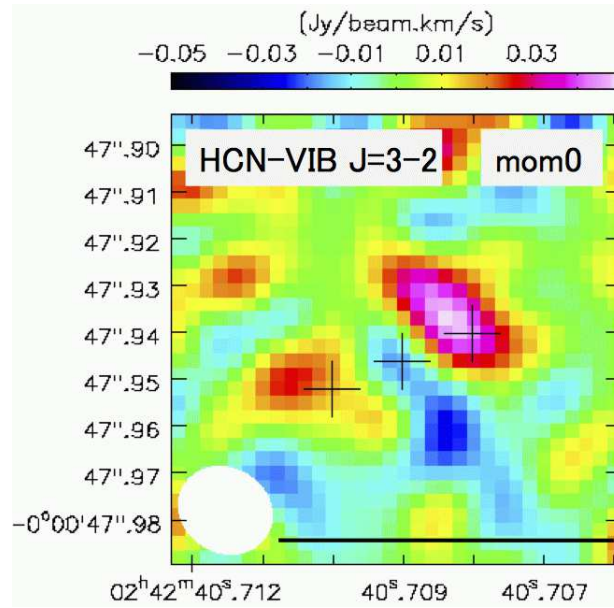


**Figure 15.** HCN-VIB J=3–2 line moment 0 map. Only signals at  $V=1170\text{--}1430\text{ km s}^{-1}$  ( $V_{\text{sys}} + [40\text{--}300]\text{ km s}^{-1}$ ) are integrated, to avoid possible contamination from the bright  $\text{HCO}^+$  J=3–2 emission line. The rms noise is  $0.010\text{ (Jy beam}^{-1}\text{ km s}^{-1})$ . The three crosses are E-peak, C-peak, and W-peak, from left to right. Signal detection with  $\sim 4.8\sigma$  (white spot) is seen at the northwestern side of the C-peak (close to the W-peak). The horizontal black bar at the lower right corresponds to 5 pc at the distance of NGC 1068. Beam size is shown as a filled circle in the lower-left region.

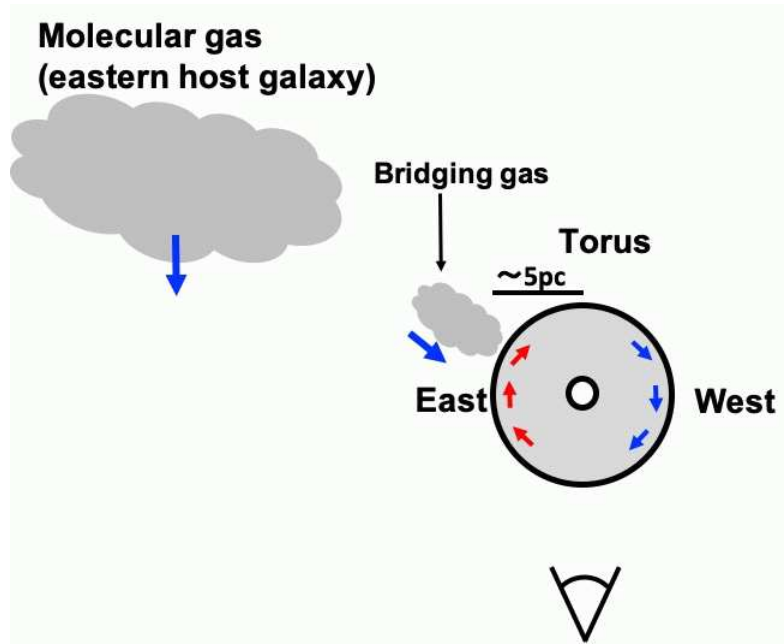


**Figure 16.** Schematic diagram of molecular gas outside the eastern torus. East is to the left and west is to the right. We are seeing from the bottom. Blue and red arrow means blueshifted and redshifted motion, with respect to the systemic velocity, respectively. Molecular gas in the eastern host galaxy is at a far side from us and is blueshifted. A blueshifted bridging molecular clump exists just outside the eastern torus. Torus outer part is redshifted at the eastern side and blueshifted at the western side.

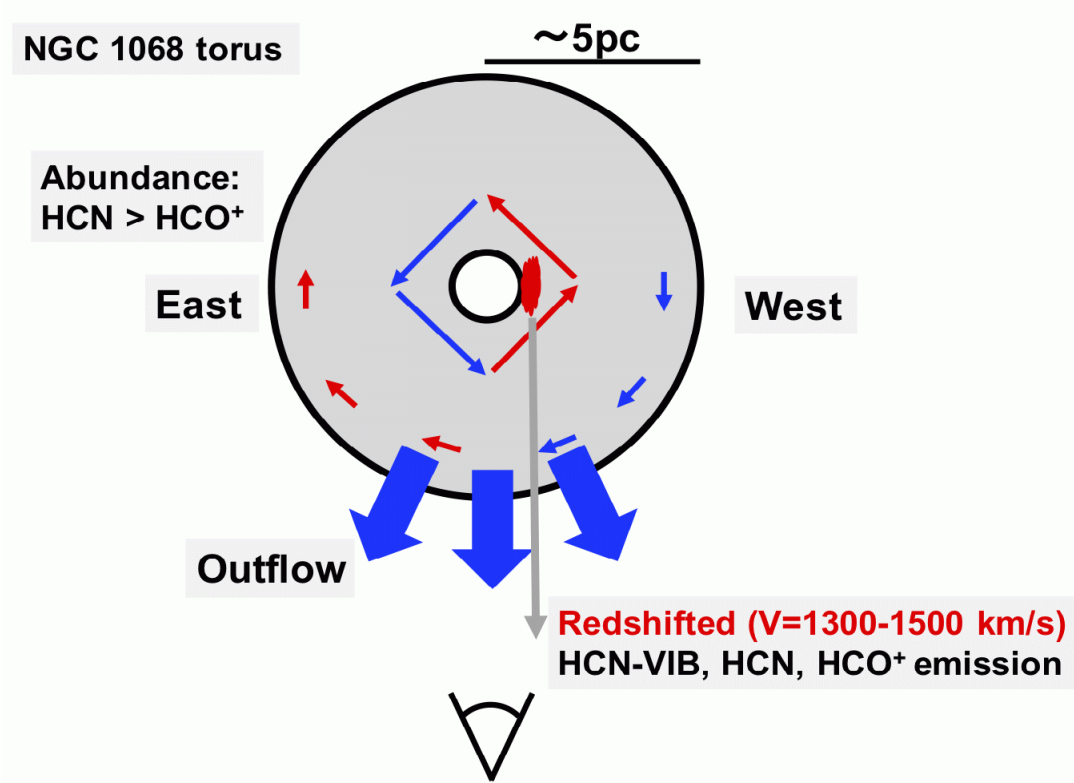


**Figure 17.** Schematic diagram of the NGC 1068 torus at  $\lesssim 5$  pc scale. East is to the left and west is to the right. We are seeing the torus from the bottom. An innermost almost-Keplerian rotating (thin long arrow) component and an outer very slowly counter-rotating (thin short arrow) component are present. Blue and red mean blueshifted and redshifted motions, respectively. (The length of the arrow is just for presentation purpose and is not scaled to actual velocity.) Dense molecular outflow (thick blue arrow) toward our direction is indicated from the blueshifted absorption wings of HCN J=3–2 and HCO<sup>+</sup> J=3–2 lines in the beam-sized C-peak spectra. The redshifted ( $V = 1300\text{--}1500\text{ km s}^{-1}$  or  $V_{\text{sys}} + [170\text{--}370]\text{ km s}^{-1}$ ) HCN-VIB J=3–2, HCN J=3–2, and HCO<sup>+</sup> J=3–2 emission lines come from the innermost northwestern torus (red filled region). Higher abundance of HCN than HCO<sup>+</sup> is suggested throughout the torus.

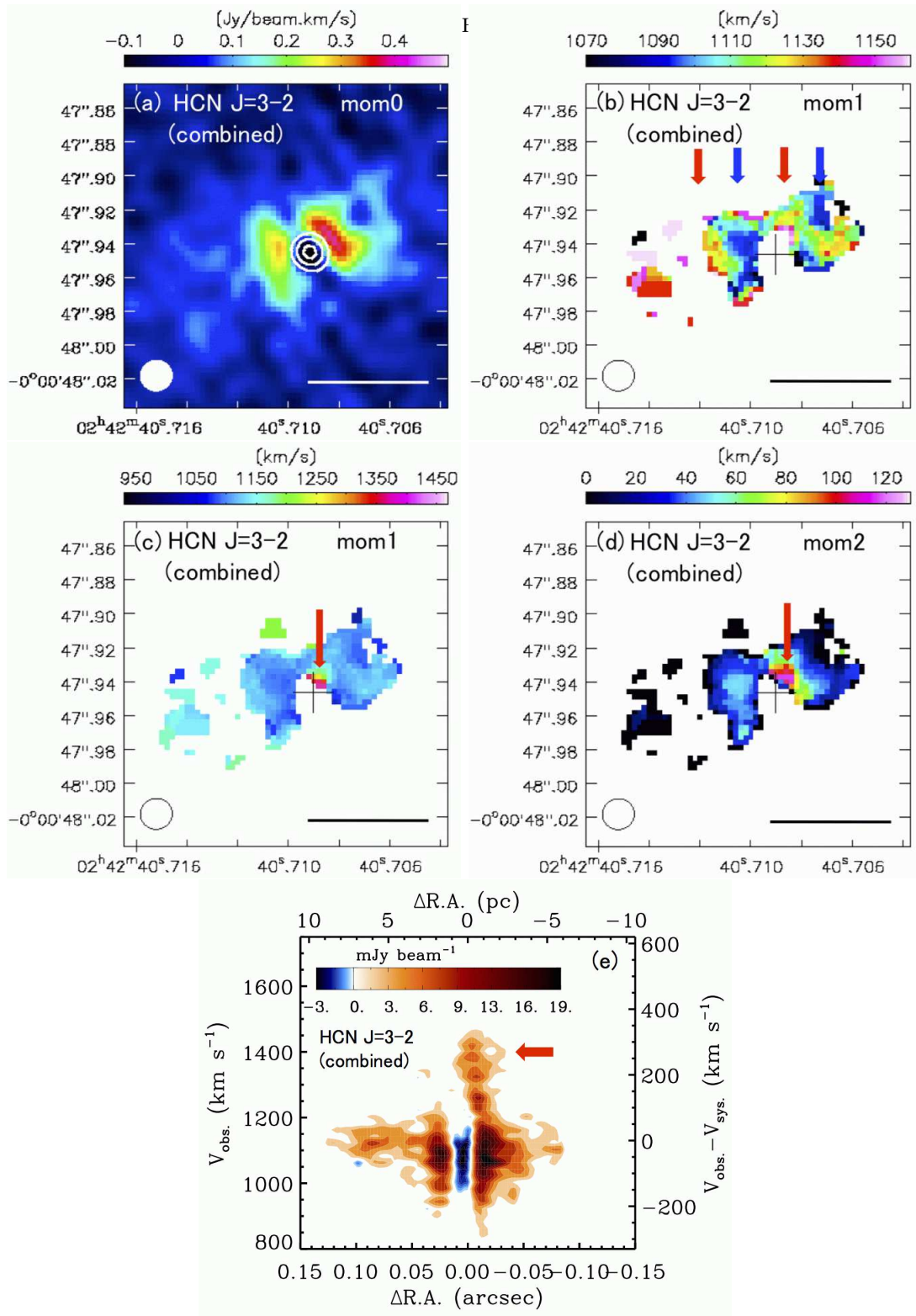


**Figure 18.** (a-d): Moment 0, 1, and 2 maps of HCN J=3-2 line in the combined data (our Cycle 6 and Cycle 5 data by Impellizzeri et al. (2019)). In (a) moment 0 map, the rms noise level is 0.030 (Jy beam<sup>-1</sup> km s<sup>-1</sup>). For (b,c) moment 1 maps, figures with two velocity display ranges are shown, following Figures 2 and 3 for our Cycle 6 data. The meanings of white contours, black cross, thick blue and red downward arrows, horizontal white or black bar, and filled or open circle in the lower-left region, are the same as those in Figures 2 and 3. An appropriate cutoff ( $\sim 5\sigma$ ) is applied to moment 1 and 2 maps in (b-d) so that they are not dominated by noise. (e): Position velocity diagram of HCN J=3-2 line along PA = 115°, displayed in the same manner as Figure 13a.

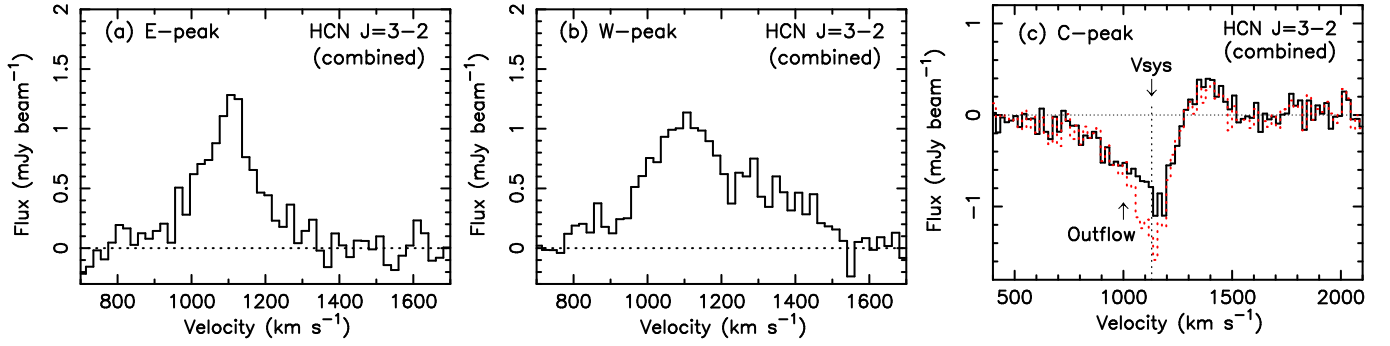


**Figure 19.** Spectra of HCN J=3–2 line at the (a) E-peak, (b) W-peak, and (c) C-peak, within the beam size ( $0''.019 \times 0''.018$ , PA =  $-79^\circ$ ), in the combined data. In all plots, the abscissa is optical LSR velocity (in  $\text{km s}^{-1}$ ) and the ordinate is flux density (in  $\text{mJy beam}^{-1}$ ). The thin horizontal dotted straight line indicates the zero flux level. In (c), the black solid line represents raw data and the red dotted line is data corrected for possible emission contamination from the innermost torus, the same as in Figure 6 (see §4.7). The systemic velocity at  $V_{\text{sys}} = 1130 \text{ km s}^{-1}$  and a blueshifted broad absorption tail at  $750\text{--}1100 \text{ km s}^{-1}$  ( $V_{\text{sys}} - [30\text{--}380] \text{ km s}^{-1}$ ) are indicated as a vertical dotted line with the note of “ $V_{\text{sys}}$ ” and an upward arrow with the note of “Outflow”, respectively.

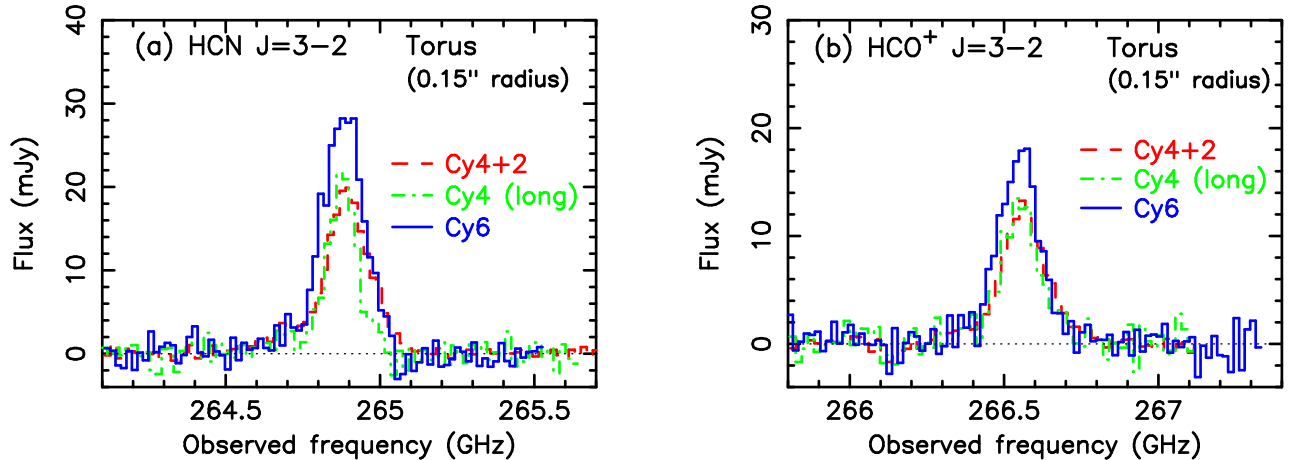


**Figure 20.** Comparison of molecular emission line profile at the AGN torus position within a  $0''.15$  (or  $\sim 10.5 \text{ pc}$ ) radius circular region centered at the C-peak ( $02^{\text{h}} 42^{\text{m}} 40.709^{\text{s}}$ ,  $-00^\circ 00' 47.946''$ ). (a): HCN J=3–2. (b):  $\text{HCO}^+$  J=3–2. The abscissa is observed frequency (in GHz) and the ordinate is flux density (in mJy). The thin horizontal dotted straight line indicates the zero flux level. Blue solid line: Cycle 6 data. Green dash-dotted line: Cycle 4 long baseline data only (Imanishi et al. 2018a). Red dashed line: Cycles 4 and 2 combined data with both long and short baselines (Imanishi et al. 2018a).